High-Fidelity Explicit Large Eddy Simulations of Airflows Inside Buildings Using the Immersed Boundary Method and Orthogonal Grids

Elyas Larkermani[a,b*], Hans Bihs[b], Grégoire Winckelmans[c], Bernhard Müller[a], Laurent Georges[a]

[a]Department of Energy and Process Engineering (EPT), Norwegian University of Science and Technology (NTNU), Gløshaugen campus, Trondheim, Norway

[b]Department of Civil and Environmental Engineering, Norwegian University of Science and Technology (NTNU), Trondheim, Norway

[c]Institute of Mechanics, Materials, and Civil Engineering (iMMC), Université Catholique de Louvain (UCLouvain), Louvain-la-Neuve, Belgium

Abstract

Large Eddy Simulation (LES) can be performed using general-purpose flow solvers such as Fluent or OpenFOAM. These solvers typically require regular grids with high orthogonality and low skewness for explicit LES. Consequently, most existing LES studies of indoor airflows rely on structured grids. Given this grid constraint, this paper presents a novel framework that demonstrates how the unique characteristics of indoor airflows make orthogonal, non-body-conformal grids a suitable choice for high-fidelity explicit LES in buildings. Firstly, orthogonal grids enable more accurate spatial discretization than general-purpose flow solvers, enhancing the precision of scale-resolving simulations. Secondly, staggered grid arrangements ensure pressure-velocity coupling without introducing artificial numerical dissipation. Thirdly, indoor airflow simulations often involve relatively moderate Reynolds numbers and localized geometrical complexity, making the Immersed Boundary Method (IBM) particularly suitable for handling solid boundaries. IBM eliminates the need for complex re-meshing techniques required for body-conformal grids, thereby facilitating simulations of airflow disturbances caused by moving objects, such as doors or human movement. Our main contribution is to define and validate this framework, as well as to test it by modifying an existing incompressible flow solver, REEF3D, originally designed for hydrodynamics. We evaluate the performance of this method through a series of benchmark tests relevant to indoor airflows, including assessments of airflows generated by sliding doors.

Keywords: Airflow inside buildings, Immersed boundary method, High-resolution Large Eddy Simulation, Finite difference

Nomenclature

Re Reynolds number

Re_τ Frictional Reynolds number

Re_θ Reynolds numbers based on the momentum thickness

Re_{δ^*} Reynolds numbers based on the displacement thickness

Sc Turbulent Schmidt number

α Thermal diffusivity

* Corresponding author.
Telephone: +47 73592036
E-mail address: elyas.larkermani@ntnu.no.
Postal address: Kolbjørn Hejes v 1B, NO-7491, Trondheim, Norway.

α_t Turbulent thermal diffusivity

β Thermal expansion coefficient

Δ Grid spacing

δ^* Displacement thickness

γ Stretching factor

υ Kinematic viscosity

ω Vorticity

ϕ Generic discrete quantity

ρ Density

θ Momentum thickness

S Resolved scale strain rate tensor

$\boldsymbol{u}$ Velocity field

C Tracer mass concentration

C_D Drag coefficient

C_L Lift coefficient

C_w WALE coefficient

g Gravitational acceleration

L Characteristic length

N Total number

p Static pressure

T Temperature

t time

U Characteristic velocity

u, v, w Cartesian velocity components

$\hat{u}$ Intermediate velocity

U^+ Normalized mean streamwise velocity

u_τ Shear velocity

V Volume

x, y, z Cartesian coordinates

y^+ Dimensionless distance to the wall

1 Introduction

Indoor environments in buildings should be comfortable and healthy for users. Air distribution in these enclosed environments is crucial with regard to thermal comfort and indoor air quality (IAQ). For instance, ventilation airflows are strictly restricted and controlled to reduce the energy use of buildings and the resulting greenhouse gas (GHG) emissions. Nevertheless, IAQ should be guaranteed so that advanced ventilation strategies are continuously improved. In hospitals, clean rooms, and public transportation, the dispersion of contaminants and pollutants is of major importance [1, 2]. Interest in the airborne spread of viruses and contaminants has increased drastically as a result of the COVID-19 pandemic [3].

Many modeling and simulation approaches have been extensively used to understand the physics of airflows inside buildings or to support the design of ventilation, space heating, or cooling strategies [4]. Nevertheless, there are significant variations in terms of modeling. In building performance simulation (BPS) tools (such as IDA-ICE, EnergyPlus, and TRNSYS), the conventional room models do not compute airflows: the air velocity is not considered, and the temperature and the concentration of pollutants are assumed to be constant in each room. Only airflows between rooms or to the outdoor environment are computed by BPS tools using *ventilation network approaches* [5]. Although simple, these approaches can successfully tackle specific flow problems, such as supporting the design of natural ventilation systems. Two alternatives are used to study airflows inside rooms (or complex flow patterns between rooms): so-called *zonal model*s and the *computational fluid dynamics* (CFD) approach. Zonal models are an intermediate between the conventional room model in BPS and CFD [6, 7]. The room is subdivided into a limited number of control volumes, where semi-empirical laws enable the computing of the fluxes between the volumes. Alternatively, zonal models can be considered as simplified CFD computation, such as coarse grid CFD or fast fluid dynamics (FFD) [8]. These zonal models are not computationally expensive, but neither are they universal, so they must be validated for specific applications and may fail outside them. Therefore, CFD is the only general simulation tool to analyze airflows inside buildings. CFD aims to numerically solve the governing equations of fluid dynamics – namely, the Navier-Stokes equations – on a computational grid. The complexity of this approach is strongly related to the *turbulence phenomenon*, which originates from the non-linear convective terms of the momentum equation in the Navier-Stokes governing equations. Turbulence generates flow structures with a broad spectrum of length and time scales. It is then worth summarizing the state-of-the-art turbulence modeling for the specific field of airflows inside buildings.

Reynolds-averaged Navier-Stokes (RANS) turbulence models remain the most widely used framework for simulating airflows in buildings due to their computational efficiency. These models average the effects of turbulence over time to represent turbulent mixing. While RANS can predict steady-state airflows inside rooms with meshes comprising millions of points or even less, a significant portion of flow physics is modeled rather than resolved. Popular models for airflows in buildings are two-equation turbulence models, e.g., the $RNG\ k-\varepsilon$, low Reynolds number $k-\varepsilon$, and $SST\ k-\omega$ models. For instance, the $RNG\ k-\varepsilon$ model generally performs best for building airflows, whereas the *Realizable* $k-\varepsilon$ model is more suited for buoyant plumes [9]. Therefore, the RANS turbulence models are not universal, and some unsteady flow phenomena are intrinsically difficult or impossible to capture using the RANS modeling approach [10]. Despite these limitations, RANS simulations heavily rely on user expertise to achieve accuracy, particularly in generating appropriate meshes and selecting suitable turbulence models [9, 11]. Therefore, high-fidelity CFD is valuable in building science, where most of the flow physics is captured by the computational mesh and a more limited part is modeled.

Large eddy simulation (LES) and *direct numerical simulation* (DNS) provide superior insights by resolving key turbulent features. DNS, which directly resolves all spatial and temporal scales of turbulence, remains an incomparable source of information for understanding flow physics in fundamental research. However, its computational cost is significant and depends on the flow type and Reynolds number. For homogeneous isotropic turbulence, the total computational cost of DNS scales with Re^3 [12], which makes it prohibitive for high Reynolds number flows. It is the main argument against using DNS in many real-life applications – typically in aeronautics but also in building environments. Nonetheless, the growing availability of computational resources has enabled DNS to be applied to specific building scenarios, such as jets, plumes [13], bidirectional airflows through large vertical openings [14], or micro-environments, using billions of grid points.

LES, in contrast, resolves large turbulent structures while modeling subgrid-scale (SGS) eddies, which are smaller and more universal. This approach enables LES to capture detached flows and flows where turbulence mixing is dominant, which RANS often struggles to model. In addition, it can provide a direct prediction of the turbulent intensity and can be adopted in situations where the flow is transitional [15] or not fully developed [16]. However, the near-wall resolution required for wall-resolved LES can approach that of DNS. This is a major limitation of LES and makes it prohibitive in many building applications, such as design. Some earlier studies, such as Van Hooff et al. [17], demonstrated the advantages of LES over RANS for cross-ventilation in indoor airflows, but many earlier LES studies for building airflows suffered from overly coarse grids [18], in the same order of magnitude as using RANS.

Hybrid RANS-LES approaches are designed to overcome the limitations of RANS and LES when used independently by combining the strengths of both methods. One prominent type of hybrid method is *Detached Eddy Simulation* (DES), originally introduced by Spalart et al. [19]. DES belongs to the category of non-zonal hybrid RANS-LES approaches, where the transition between RANS and LES regions is based on the grid resolution and flow characteristics [20]. DES typically applies RANS modeling near walls, where the grid resolution is insufficient for LES, and transitions to LES in regions of separated or bulk turbulence, where large-scale eddies dominate the flow. Although DES shows potential for building airflows, the DES performance has not been properly documented so far in the context of airflows inside buildings [10].

LES can be performed using different strategies that can be categorized according to several criteria. Two main aspects are discussed here:

- The first distinction can be made based on the interaction between the spatial discretization error and the SGS model. In LES, the energy cascade between the different flow length scales should be properly reproduced. The discretization scheme for the convective term can introduce artificial dissipation that interacts with the energy cascade by removing kinetic energy. In *explicit LES*, the dissipation related to the subgrid scales is almost entirely performed by the SGS model. This requires the artificial dissipation from the spatial discretization of the convective term in the momentum equation to be null or limited, typically using a central scheme. To guarantee the unconditional stability of a pure central scheme in an under-resolved simulation, the discrete kinetic energy must be conserved [21]. In *implicit LES*, the artificial dissipation of the spatial discretization scheme is tailored to act as a consistent SGS model [22].
- The second distinction can be made between *body conformal* and *non-body conformal* grids [23]. Body conformal meshes follow the surface geometry of the objects exactly, and may result in complex structured or unstructured grids for complex geometries. Conversely, non-body conformal grids do not need to follow the surface geometry, so dense regular grids, such as orthogonal or cartesian grids, can be used. The presence of walls is then treated in a specific way using immersed boundary methods (IBM) [23]. Orthogonal grids with IBM make it possible to easily generate meshes for complex geometries.

Most existing LES for airflows inside buildings resort to explicit LES using body conformal grids, either structured or unstructured [15, 17]. Then, artificial dissipation should be limited, which is a main reason for using (almost fully) structured grids with good orthogonality and limited skewness. Consequently, some strong constraints on the grid quality should be followed when high-fidelity LES is performed using general-purpose flow solvers such as Fluent or OpenFOAM [10].

Given this strong constraint on the mesh, the main contribution of the paper is to show that airflows inside buildings have specific features that make non-body conformal orthogonal grids an interesting alternative to the common general-purpose flow solvers. For this purpose, the opportunities introduced by non-body conformal orthogonal grids are listed and properly discussed, such as the simpler implementation of high-accurate spatial discretization. The second contribution is to introduce some adaptations of a specific incompressible flow solver based on orthogonal grids to perform explicit LES for airflows inside buildings, including moving objects, and to investigate its performance using several relevant benchmarks.

2 LES using orthogonal grids

Airflows in buildings have specific features. The flow can be laminar, transitional, or turbulent, sometimes simultaneously in different regions of the same room. They are characterized by lower Reynolds numbers than aerodynamic applications. Generally, airflows inside buildings are less dependent on geometry details than in aerodynamic applications. Moreover, their internal flow dynamics appearing in the bulk are as important as in environmental flows – e.g., due to the buoyancy effect. These flows can be assumed to be incompressible.

Employing orthogonal grids introduces the following advantages and challenges. Some of these advantages are particularly relevant for the simulation of airflows inside buildings:

- In general-purpose flow solvers, the standard second-order central scheme uses a linear reconstruction of the flow variables to the cell faces. Its numerical stencil thus resorts to five points in each spatial direction when applied on a structured mesh. Using a solver tailored for orthogonal grids, extending

the numerical stencil to more points makes it easy to improve the numerical accuracy – for instance, to minimize the truncation error. In transitional flows, minimized dispersion errors can be crucial to correctly capture the advection of flow structures. It is also interesting to mention that orthogonal grids ease the application of line-iterative techniques and geometrical multigrid solvers.

- Due to the anisotropy of the velocity field in boundary layers, the density of grid points can be higher using non-body conformal grids than boundary-fitted meshes for high Reynolds number flows. Several factors may counterbalance this effect. Firstly, given the low Reynolds numbers in airflows inside buildings, this effect should be less critical than in aerodynamic applications. Secondly, in many indoor applications, the geometrical complexity is localized (e.g., around occupants and air supply terminals), which means that grid refinement is possible with a non-uniform orthogonal mesh along walls for the rest of the room, see Figure 1. Typically, the shape of the room can most often be approximated by a combination of boxes. In other words, the mesh can be body conformal on most of the boundaries and non-body conformal in the limited volume where the geometry is complex. Thirdly, the evaluation of the forces on surfaces is less important in building applications than in aerodynamic applications as long as the relevant physical phenomenon for ventilation is captured (such as the location of the flow detachment). Finally, the grid resolution near the wall can be very demanding in wall-resolved LES. However, wall functions have been improved in wall-modeled LES [24-26]. This enables a significant decrease in the grid resolution near the wall, which can enable the use of non-body conformal grids at high Reynolds. For instance, wall functions that better integrate the buoyancy effect have recently been developed [27].
- The prevalent eddy viscosity models in explicit LES – the Smagorinsky and the wall-adapting local eddy-viscosity (WALE) SGS models [28] – tend to be too dissipative on the large resolved scales of the flow, even when applied with the dynamic procedure [29]. Multiscale SGS models apply a spatial filtering procedure to discriminate between large and small resolved scales. In this way, the SGS dissipation is only applied on the smallest resolved scales, while leaving the largest ones untouched [30]. This ensures that the SGS model remains inactive in the laminar and transitional part of the flow. Discrete spatial filters can be adopted with both unstructured and structured meshes, but the performance of the filter can be characterized more easily on an orthogonal mesh [31].
- The immersed boundary method can consider moving objects without having to re-mesh at each time step [23]. This is a clear advantage compared to a body-fitted mesh, where the procedure to analyze moving objects can be demanding. IBM enables the simulation to move objects more easily in building applications, such as moving persons and transient operation of doors and windows.
- The final advantage does not necessarily need to be selected but can lead to simplifications. It is possible to use a staggered arrangement of the incompressible flow variables using an orthogonal mesh [32]. With a staggered grid, there is a strong coupling of the pressure and velocity fields such that no specific numerical treatment is needed to avoid the checkerboard problem (also called odd-even decoupling). Numerical treatment of the odd-even decoupling may introduce numerical dissipation by defining an interpolation scheme for the pressure [33], whilst staggered grids are free of them. Finally, it is possible to define a convective scheme that exactly conserves discrete kinetic energy using a staggered grid, which is beneficial for explicit LES [21, 34].

Some previous studies have already applied some of these advantages of orthogonal grids to perform LES of airflows inside buildings. However, these studies lack an extended discussion of the pros and cons of orthogonal grids, covering the five points discussed earlier.

Kempe et al. [35] introduced a numerical scheme for LES of indoor airflows using orthogonal staggered grids and IBM for stationary objects. However, their spatial discretization scheme is a standard second-order central scheme. Therefore, they do not exploit the capacity to improve spatial discretization. On the contrary, Morozova et al. [36] resort on a fourth-order symmetry preserving finite volume method on an orthogonal staggered mesh to perform LES of airflows inside buildings. However, the treatment of complex geometries is not discussed in their work. It is worth mentioning that these two studies introduced their methods to perform high-fidelity LES at moderate computational efforts.

IBM on orthogonal grids has been previously used to simulate contaminant transport in buildings. Mao and Celik [37] used orthogonal staggered grids along with a standard second-order method for the spatial discretization to perform (U)RANS simulations. Choi and Edwards investigated contaminant transport by

human movement using LES [38, 39]. They resort to a second-order low-diffusion scheme for spatial discretization on collocated orthogonal grids. It is worth noting that the IBM has also been used in unstructured flow solvers to study body movement and pollutant dispersion in buildings, as seen in works like Löhner et al. [2] and Saarinen et al. [40] using ANSYS CFX. To avoid confusion, it is important to note that orthogonal grids are not the prerequisite for implementing IBM; quite the opposite, it is IBM that facilitates the use of orthogonal grids, especially with complex geometries.

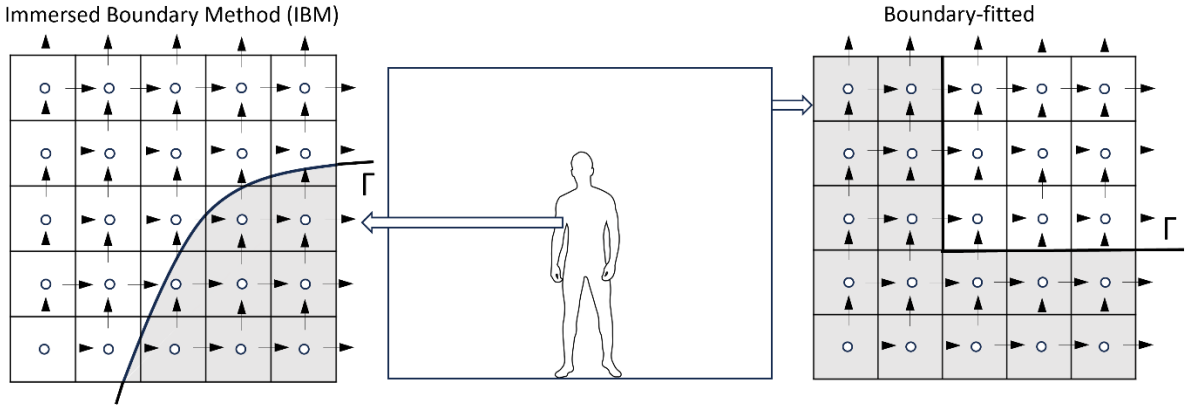

Figure 1. 2-D representation of a staggered mesh with a wall boundary Γ and two layers of ghost points in the grey zone: pressure points are indicated using circles, while velocity components are shown using arrows.

Compared to these studies, the original contribution of our work is a broader integration of the benefits offered by orthogonal grids, as shown in Table 1. It introduces an innovative and accurate central finite difference scheme in conjunction with IBM on a staggered orthogonal mesh that can properly model moving objects.

Table 1. Comparison of the features of the different CFD works based on orthogonal grids or IBM in the field of indoor airflows.

References	Type	Larger Stencil	Orthogonal	Multiscale SGS	IBM	Staggered grid
Kempe et al. [35]	LES	☒	☑	☒	☑	☑
Morozova et al. [36]	LES	☑	☑	☒	☒	☑
Mao et al. [37]	RANS	☒	☑	☒	☑	☑
Löhner et al. [2]	LES	☒	☒	☒	☑	☒
Saarinen et al. [40]	LES	☒	☒	☒	☑	☒
Present	LES	☑	☑	☑	☑	☑

3 Numerical method

In the remainder of the article, the framework introduced in Section 2 is applied to adapt an existing incompressible flow solver with staggered orthogonal grids to high-fidelity LES for airflow inside buildings, including moving objects and accurate spatial discretization.

3.1 Governing equations

The incompressible Navier-Stokes equations for a Newtonian fluid with constant physical properties are considered. The Boussinesq approximation accounts for the change of density resulting from a temperature change, while thermal radiation between surfaces is neglected (as air can be assumed as a transparent medium in buildings). Heat transfer occurs only via conduction and convection. Based on these assumptions, the governing equations can then be written in the following form:

$$\nabla \cdot \boldsymbol{u} = 0 \tag{1}$$

$$\frac{\partial \boldsymbol{u}}{\partial t} + \nabla \cdot (\boldsymbol{u}\boldsymbol{u}) = -\frac{\nabla(p - \rho_0 \boldsymbol{g}.\boldsymbol{z})}{\rho_0} + \nabla \cdot \left(\upsilon(\nabla \boldsymbol{u} + (\nabla \boldsymbol{u})^T)\right) - \beta \boldsymbol{g}(T - T_{\text{ref}}) \quad (2)$$

$$\frac{\partial T}{\partial t} + \nabla \cdot (\boldsymbol{u}T) = \nabla \cdot (\alpha \nabla T) + Q \quad (3)$$

where $\boldsymbol{u} = (u, v, w)$ is the velocity vector in cartesian coordinates $\boldsymbol{x} = (x, y, z)$. p represents the pressure field, T is the temperature, ρ_0 the reference density. Here, parameters υ and α are the kinematic viscosity and the thermal diffusivity, respectively. They can be assumed constant for airflows inside buildings. The last term in Equation (2) is the buoyancy term, where $\beta = 1/T_{\text{ref}}$ is the thermal expansion coefficient of the air modeled as an ideal gas and g the gravitational acceleration. The second term on the right-hand side of Equation (3) (Q) is the heat source.

3.2 Flow solver adaptation

REEF3D [41] is an open-source parallel flow solver that was developed for hydrodynamics applications. From the start, the focus of REEF3D was to solve complex free surface dynamics through two-phase flow interface capturing. The architecture of REEF3D makes it a relevant candidate according to the framework introduced in Section 2. Firstly, the grid is orthogonal, with a one-dimensional grid stretching in each spatial direction. As shown in Figure 1, a staggered arrangement of the flow variables is adopted. Secondly, the baseline numerical stencil for the convective term involves seven points in each spatial direction, which enables the development of high-resolution schemes. The baseline scheme in REEF3D is a weighted essentially non-oscillatory (WENO) scheme, which is a fifth-order accurate scheme for linear advection problems. However, the formulation is hybrid in the sense that the mass conservation, the pressure gradient, and diffusion terms are still discretized using second-order central finite differences. REEF3D is thus formally second-order but with reduced dispersion errors using a seven-point numerical stencil to discretize convective terms. Thirdly, the fractional step method is used to enforce the discrete continuity equation [42]. Given the second-order discretization of the velocity divergence in Equation (1) and the pressure gradient in Equation (2), it leads to the resolution of a second-order Poisson equation. The Poisson equation is solved using an efficient geometric multigrid linear solver from the HYPRE library [43]. Finally, the effect of complex geometries is integrated using IBM.

The ghost cell approach is used for fixed, rigid boundaries (i.e., solid objects). This enables a sharp representation of the immersed boundaries, which is desirable, especially at high Reynolds numbers [23]. The local directional ghost cell approach of Berthelsen and Faltinsen [44] has been implemented in order to treat sharp corners accurately. The sharp-interface methods, such as cut cells and ghost cells, encounter a major challenge with boundary motion. A cell in a solid body can become part of the fluid domain during movement. The spatial discontinuity associated with the sharp immersed boundary can lead to a temporal discontinuity for cells near the boundary. Therefore, a straightforward temporal discretization of the momentum on these cells is not possible, as flow variables in these cells do not have a valid time history [23]. Therefore, an IBM based on a continuous forcing term in the momentum equation is implemented to treat moving boundaries, employing the method of Yang [45]. The forcing term is added to the momentum equation, which is solved throughout the entire domain. This term is calculated in each velocity grid point in the solid body. However, a smooth transition is applied across a few grid cells on both sides of the solid boundary to eliminate temporal discontinuities for cells emerging into the fluid [23]. In REEF3D, the incompressible Navier-Stokes equations are solved in parallel using domain decomposition. Partitions communicate with their neighbors using ghost cells and the message passing interface (MPI) [46].

In conclusion, REEF3D already has many of the characteristics listed in Section 2. To perform explicit LES efficiently, the flow solver should be adapted. To this end, a non-dissipative spatial discretization is developed and implemented (see Section 3.3). The default temporal discretization is high-order using the third-order explicit total variation diminishing (TVD) Runge-Kutta (RK) method with a projection step at each stage. However, a common strategy for LES and DNS is to apply an explicit time integration for the convective terms and an implicit integration for the diffusion terms. The main reason for the implicit treatment of the diffusive terms is the severe time step restriction for numerical stability in regions with substantial grid refinement, typically along the walls. As the velocity is generally very small close to the wall, the time step requirement for the explicit convective term is less severe. Therefore, REEF3D has been adapted by implementing a low-dissipative semi-implicit RK scheme (see Section 3.4). On top of that, SGS models with and without spatial

filters [30] are incorporated into REEF3D, providing an option to select a multiscale SGS model or a standard one. Additionally, the original purpose of REEF3D was hydrodynamic applications; it deals with air and water and, consequently, has significant density differences compared to the density differences created by air temperature in building applications. Therefore, REEF3D did not rely on the Boussinesq approximation, and this term needs to be implemented. The two major implementations are the central discretization scheme for the convective terms and the semi-implicit RK scheme. The other two modifications can be considered as minor.

3.3 Hybrid central finite difference

Following the notation of Vasilyev [34], two discrete operators are introduced, enabling the concise formulation of central finite difference schemes on a staggered mesh. They can be applied at both pressure and velocity points. The interpolation operator in physical space with stencil n can be applied on a field ϕ in the direction x at the grid point of index (i, j, k):

$$\bar{\phi}^{nx}|_{i,j,k} = \frac{\phi(i + n/2, j, k) + \phi(i - n/2, j, k)}{2} \tag{4}$$

The second operator is the finite difference operator of stencil n in the direction x acting on the field ϕ at the grid point of an index (i, j, k):

$$\frac{\delta_n \phi}{\delta_n x}|_{i,j,k} = \frac{\phi(i + n/2, j, k) - \phi(i - n/2, j, k)}{x(i + n/2, j, k) - x(i - n/2, j, k)} \tag{5}$$

The extension of these two operators to the other spatial directions, y and z, is straightforward. The grid point indices (i, j, k) will be omitted for these two operators in the remainder of the text to avoid any confusion with Cartesian tensor notation. From now on, the letters i and j will exclusively be used to index the spatial directions. Using these discrete operators, the standard second-order central finite difference (CDS2) of the convective term (Conv) in direction i can be expressed in the following way:

$$\mathrm{Conv}_i(u) = \frac{\partial}{\partial x_j}(u_j u_i) \approx \frac{\delta_1}{\delta_1 x_j}\left(\bar{u}_j^{1x_i} \bar{u}_i^{1x_j}\right) \tag{6}$$

Here, the Einstein summation convention is used on index j. Rivas [47] showed that this scheme has a first-order truncation error on a non-uniform grid, whilst it achieves second-order accuracy on a continuously stretched grid. According to Vasilyev et al. [34], this divergence form of the convective terms in the Navier–Stokes equations preserves the conservation of continuity and momentum at the discrete level using exact time-integration in the absence of viscous dissipation. However, kinetic energy conservation by convection may not be guaranteed using the divergence form on a non-uniform staggered grid due to the commutation error term. The conservation of discrete kinetic energy is important to perform explicit LES and to guarantee the numerical stability of central schemes in under-resolved simulations like LES. The numerical stencil of CDS2 only involves three points in each spatial direction. However, REEF3D allows finite difference schemes with a numerical stencil of up to seven points by spatial direction. This feature can be used to introduce a better numerical scheme than the standard CDS2.

Morinishi et al. [48] developed high-order finite differences on staggered orthogonal grids that conserve the discrete momentum and kinetic energy when the mesh is uniform. These schemes were extended by Vasilyev [34] to preserve good conservation properties on non-uniform grids. However, it was determined that the commutation error between discrete differencing and averaging operators was a key factor contributing to non-conservation on non-uniform meshes. So, his proposed schemes can combine fourth-order accuracy with the discrete conservation of either momentum or kinetic energy on non-uniform grids. Verstappen and Veldman [21] proposed a fourth-order finite volume method for non-uniform staggered meshes. Unlike the approach of Vasilyev [34], the scheme of Verstappen and Veldman [21] can simultaneously conserve the discrete momentum and kinetic energy on a non-uniform mesh. The coefficients of these schemes [21, 34, 48] are not adjusted locally based on the local grid-stretching as they are applied to the computational space rather than the physical space to preserve the symmetry of the discrete operator. Nevertheless, they are fourth-order accurate for a continuously stretched non-uniform grid.

One of the difficulties of implementing these fourth-order schemes is that their numerical stencil is not compact in the sense that they require high-order interpolation in the three spatial directions. This makes the

implementation of these schemes more complex and the treatment of boundary conditions more challenging, especially for complex geometries in practical engineering problems using IBM. Our goal is thus to improve the numerical accuracy of the CDS2 scheme with a scheme that keeps the numerical stencil compact so that the implementation and the treatment of boundary conditions remain simple. To this purpose, the CDS2 is improved by discretizing the convective fluxes more accurately using a symmetric seven-point stencil [49]. In contrast, the convection velocity remains unchanged and interpolated with a second-order accurate interpolation operator as in the original CDS2:

$$\mathrm{Conv}_i(u) = \frac{\partial}{\partial x_j}\left(u_j u_i\right) \approx \frac{\delta_1}{\delta_1 x_j}\left(\bar{u}_j^{1x_i}\left(\alpha_1 \bar{u}_i^{1x_j} + \alpha_3 \bar{u}_i^{3x_j} + \alpha_5 \bar{u}_i^{5x_j}\right)\right) \tag{7}$$

with α_1, α_3, and α_5 being the constant scheme coefficients, which are not adapted according to the local grid-stretching. The coefficients $\alpha_1 = 37/30$, $\alpha_3 = -8/30$, and $\alpha_5 = 1/30$ are chosen so that Equation (7) corresponds to a sixth-order central difference approximation when the convection velocity is constant. Therefore, this new scheme is termed HCDS6, where the H stands for the hybrid combination. In general, the scheme remains second-order accurate; however, it has a significantly smaller truncation error than the standard second-order central scheme (CDS2). It conserves the discrete momentum on a non-uniform mesh but not the discrete kinetic energy. For $\alpha_1 = 1$, $\alpha_3 = 0$, and $\alpha_5 = 0$, the method is degraded to CDS2, and thus, the HCDS6 only extends the numerical stencil along lines in each spatial direction, keeping the stencil compact. For instance, the new method is more compact than the fourth-order finite-difference schemes of Vasilyev [34], where the convection velocity is interpolated with a fourth-order accurate interpolation operator:

$$\mathrm{Conv}_i(u) \approx \left[\frac{9}{8}\frac{\delta_1}{\delta_1 x_j}\left\{\left(\frac{9}{8}\bar{u}_j^{1x_i} - \frac{1}{8}\bar{u}_j^{3x_i}\right)\bar{u}_i^{1x_j}\right\} - \frac{1}{8}\frac{\delta_3}{\delta_3 x_j}\left\{\left(\frac{9}{8}\bar{u}_j^{1x_i} - \frac{1}{8}\bar{u}_j^{3x_i}\right)\bar{u}_i^{3x_j}\right\}\right]_{i,j,k} \tag{8}$$

3.4 Semi-implicit time integration

An accurate and low-dissipation semi-implicit time integration scheme might be needed when the grid is well refined near the walls to perform wall-resolved LES. Therefore, the popular semi-implicit Runge-Kutta method by Le and Moin [50] has been implemented in REEF3D and requires modification of the code structure. In this temporal approach, every time step is advanced in three sub-steps, each of which uses the second-order-implicit Crank-Nicholson method to integrate the diagonal contribution of the diffusive term (Laplacian term), while the other terms are explicitly integrated using a second-order Adams-Bashforth method. The predictor-corrector technique, and the Poisson equation for the three steps are formulated as follows:

$$\begin{aligned}\frac{\hat{u}_i^m - u_i^{m-1}}{\chi_m \Delta t} + \gamma_m \frac{\delta}{\delta x_j}\left(u_j^{m-1}u_i^{m-1}\right) + \kappa_m \frac{\delta}{\delta x_j}\left(u_j^{m-2}u_i^{m-2}\right) \\ = -\frac{1}{\rho}\frac{\delta p^{m-1}}{\delta x_i} + \frac{\delta}{\delta x_j}\left[\upsilon\left(\gamma_m \frac{\delta u_j^{m-1}}{\delta x_i} + \kappa_m \frac{\delta u_j^{m-2}}{\delta x_i}\right)\right]_{i\neq j} \\ + \theta\left(\frac{1}{2}\frac{\delta}{\delta x_j}\left[\upsilon\frac{\delta \hat{u}_i^m}{\delta x_j}\right] + \frac{1}{2}\frac{\delta}{\delta x_j}\left[\upsilon\frac{\delta u_i^{m-1}}{\delta x_j}\right]\right) + g_i\left[1 - \beta\left(T^{m-1} - T_{ref}^{m-1}\right)\right]\end{aligned} \tag{9}$$

Here, the superscript m represents the sub-step number, taking values from 1 to 3. For the initial sub-step ($m = 1$), the term corresponding to $m - 2$ is disregarded. The u_i^0 and u_i^3 denote the velocities at time steps n and $n + 1$, respectively. The coefficients γ_m, κ_m and χ_m at each sub-step m are constants provided in Table 2. The coefficient θ equals 2 for $i = j$, and 1 otherwise. The second term on the right-hand side includes the non-diagonal components of the diffusive term, while the third term incorporates the diagonal components integrated using the Crank-Nicholson method.

Table 2. Coefficients for semi-implicit Runge-Kutta method.

m	χ_m	γ_m	κ_m
1	$\frac{8}{15}$	1	0
2	$\frac{2}{15}$	$\frac{25}{8}$	$-\frac{17}{8}$
3	$\frac{5}{15}$	$\frac{9}{4}$	$-\frac{5}{4}$

The resulting intermediate velocity $\hat{u}_i^m$ does not satisfy the continuity equation (Equation (1)). To obtain the new velocity u_i^m, the intermediate velocity is projected onto the space of incompressible divergence-free vector field:

$$\frac{u_i^m - \hat{u}_i^m}{\chi_m \Delta t} = -\frac{1}{\rho}\frac{\delta(p^m - p^{m-1})}{\delta x_i} \tag{10}$$

This is done by solving a Poisson equation for the pressure field, which is derived by applying the divergence to the intermediate velocity field and enforcing $\delta u_i^m / \delta x_i = 0$:

$$\frac{\delta}{\delta x_i}\left(\frac{1}{\rho}\frac{\delta(p^m - p^{m-1})}{\delta x_i}\right) = \frac{1}{\chi_m \Delta t}\frac{\delta \hat{u}_i^m}{\delta x_i} \tag{11}$$

In REEF3D, the fully parallelized bi-conjugate gradients stabilized (BiCGStab) algorithm [51] solves the Poisson pressure equation by using geometric multigrid preconditioning provided by the high-performance solver library, HYPRE [52].

The time integration of the energy equation is done using a single step at each RK stage:

$$\frac{T^m - T^{m-1}}{\Delta t} + \gamma_m \frac{\delta}{\delta x_j}\left(u_j^{m-1} T^{m-1}\right) + \kappa_m \frac{\delta}{\delta x_j}\left(u_j^{m-2} T^{m-2}\right) = \frac{1}{2}\left(\frac{\delta}{\delta x_j}\left[\alpha \frac{\delta T^{m-1}}{\delta x_j}\right] + \frac{\delta}{\delta x_j}\left[\alpha \frac{\delta T^{m}}{\delta x_j}\right]\right) \tag{12}$$

A similar approach is applied for the advection of a passive scalar, such as the concentration of a gaseous pollutant. For the viscous terms and the pressure term, the second-order central differential scheme is adopted – for example:

$$\frac{\partial}{\partial x_j}\left[\frac{\partial u_i}{\partial x_j}\right] \approx \frac{\delta_1}{\delta_1 x_j}\left\{\frac{\delta_1 u_i}{\delta_1 x_j}\right\} \tag{13}$$

3.5 Enhanced direct forcing IBM

To distinguish between the fluid and the solid object, the direct-forcing immersed boundary method is employed. This method operates within the one-fluid framework, as described in [45], which treats air and solid phases uniformly using the Navier-Stokes equations. The governing equations (Equations (1)-(3)), are extended to incorporate a forcing term $\boldsymbol{f}$ in the momentum equation to account for the boundary conditions at the fluid-solid interface [45]:

$$\frac{\partial \boldsymbol{u}}{\partial t} + \nabla.(\boldsymbol{u}\boldsymbol{u}) = -\frac{\nabla(p - \rho_0 \boldsymbol{g}.\boldsymbol{z})}{\rho_0} - \beta \boldsymbol{g}(T - T_{\mathrm{ref}}) + \boldsymbol{f} \tag{14}$$

The forcing term $\boldsymbol{f}$ is defined differently based on the phase (solid or fluid):

$$f = \begin{cases} \dfrac{\partial \boldsymbol{P}(\boldsymbol{u})}{\partial t} + \boldsymbol{P}(\boldsymbol{u}) \cdot \nabla \boldsymbol{P}(\boldsymbol{u}) + \dfrac{\nabla(p - \rho_0 \boldsymbol{g}.\boldsymbol{z})}{\rho_0} + \beta \boldsymbol{g}\left(T - T_{ref}\right) & \varphi_s < 0 \\ \nabla.\left(\upsilon(\nabla \boldsymbol{u} + (\nabla \boldsymbol{u})^T)\right) & \varphi_s > 0 \end{cases} \tag{15}$$

where φ_s is the signed distance function defining the structure, with $\varphi_s < 0$ indicating the solid phase and $\varphi_s > 0$ indicating the fluid phase. The projection operator $\boldsymbol{P}(\boldsymbol{u})$ is employed to ensure the velocity field satisfies the divergence-free condition in the solid phase.

The rigid body velocity field is approximated as $\boldsymbol{P}\left(u_i^{m-1}\right) = u_i^{m-1}$. Using explicit time integration, as shown in Equation (9), the forcing term at each time step is calculated according to the Equation (16). This term is smoothly smeared out across the interface using a smoothed Heaviside function (H):

$$f^m = H(\varphi_s^m) \cdot \frac{\boldsymbol{P}(u_i^m) - \hat{u}_i^m}{\Delta t} \tag{16}$$

Heaviside function $H(\varphi_s)$ provides a smooth variation of properties across the interface where φ_s is the level set function defining the shortest distance to the interface.

$$H(\varphi_s) = \begin{cases} 0 & \text{if } \varphi_s < -\epsilon \\ \frac{1}{2}\left(1 + \frac{\varphi_s}{\epsilon} + \frac{1}{\pi} sin\left(\frac{\pi\varphi_s}{\epsilon}\right)\right) & \text{if } |\varphi_s| \leq \epsilon \\ 1 & \text{if } \varphi_s > \epsilon \end{cases} \quad (17)$$

The interface thickness is defined as $\epsilon = 0.6\Delta x$, where Δx is the characteristic local grid size [53]. For the sake of the conciseness, the time integration of Equation (16) and the level set method are given in the Appendix.

4 Results

In this section, five benchmark tests conducted using the REEF3D flow solver are presented. These tests serve to showcase the capabilities and effectiveness of the current numerical approach. They include four generic benchmarks: the DNS of a wall-attached cube, the DNS and LES of flow past a sphere, and the LES of turbulent channel flow. Finally, one benchmark that is specific for airflow inside buildings is considered with a moving object. For this purpose, the LES of the transitional flow generated by a sliding door is analyzed.

4.1 Flow past a wall-attached cube

The flow around a wall-attached solid cube is a simple geometry that offers valuable insights into the interaction between a boundary layer and complex bodies immersed within it. Although the scope of this paper is about indoor airflows, the flow around square cylinders with varying aspect ratios is also an important test case in environmental applications, enabling a simulation of airflow dynamics around simplified architectural structures [54, 55]. The sharp corners of the cube challenge the performance of the IBM using the ghost cell approach. In REEF3D, the local directional ghost cell approach [38] was introduced to solve this challenge. The enhanced direct forcing IBM implemented in the REEF3D is also adopted to account for the influence of solid boundaries in the Navier-Stokes equations.

The wall-attached cube is a geometric solid positioned in a zero-pressure gradient boundary layer. The computational setup is identical to the one used by Diaz-Daniel et al. [56] in their DNS of wall-attached cube immersed in laminar and turbulent boundary layers. For the sake of simplicity, only the laminar case at $Re_H = 500$ is investigated here, where the inlet boundary condition is defined by the Blasius laminar boundary layer profile. The cube is located at a distance $9H$ from the inlet, where H is the cube height. The coordinate system is aligned with the front plane of the cube where the origin is located at $x = 0$. A no-slip boundary condition is applied at the bottom wall, while a homogeneous Neumann condition is imposed at the top boundary. In the spanwise direction, the periodic boundary condition is adopted to simulate an infinite array of cubes. The computational domain size and grid resolution are summarized in Table 3. Re_θ and Re_{δ^*} are based on the momentum thickness θ and the displacement thickness δ^*, respectively, for the freestream velocity U_∞.

Table 3. Computational domain size and mesh resolution for DNS of the wall-attached cube.

Re_H	Re_θ	Re_{δ^*}	$\frac{L_x}{H} \times \frac{L_y}{H} \times \frac{L_z}{H}$	$N_x \times N_y \times N_z$	$\frac{\Delta y_{wall}}{H}$	$\frac{\Delta y_{top}}{H}$	$\frac{\Delta t U_\infty}{H}$	$\frac{TU_\infty}{H}$
500	68	175	$35 \times 15 \times 8$	$336 \times 144 \times 186$	0.02	0.68	$1.516e-3$	10000

A uniform grid with a cell size of $0.02H$ is created in a rectangular refinement area measuring $[2H \times 2H \times 2H]$ around the cube. The cells are elongated with a growth ratio of 1.2 in the wall-normal direction from the refined zone to the top boundary of the domain, ensuring that the largest cell size does not exceed $0.68H$. A smaller growth ratio of 1.05 is set in streamwise and spanwise directions from the focus zone up to the lateral boundaries of the domain, where the maximum cell size is $0.2H$ and $0.5H$ in x and z directions, respectively. The flow statistics are time-averaged over a period T following a long initial transient period until the flow is statistically steady-state.

The time-averaged streamwise velocity contours with mean flow streamlines around the wall-attached cube are illustrated in Figure 2. A deceleration region is created as the flow encounters the cube front plane. The

flow accelerates gradually along the cube's leading face, with a well-behaved velocity gradient near the wall. A mild separation occurs at the leading edge, followed by a thin boundary layer along the cube top face. In the wake region behind the cube, vortices and disturbances are less pronounced than higher Reynolds numbers, resulting in a more organized flow structure. The mean-flow streamlines show a closed recirculation region in front of the cube (Figure 2, left) surrounded by a horseshoe vortex system upstream and around the wall-attached cube (Figure 2, right). The contours of time-averaged streamwise velocity show that the flow structures align remarkably well with benchmark DNS data, thereby underlining the robustness and reliability of the immersed boundary method implemented in the flow solver.

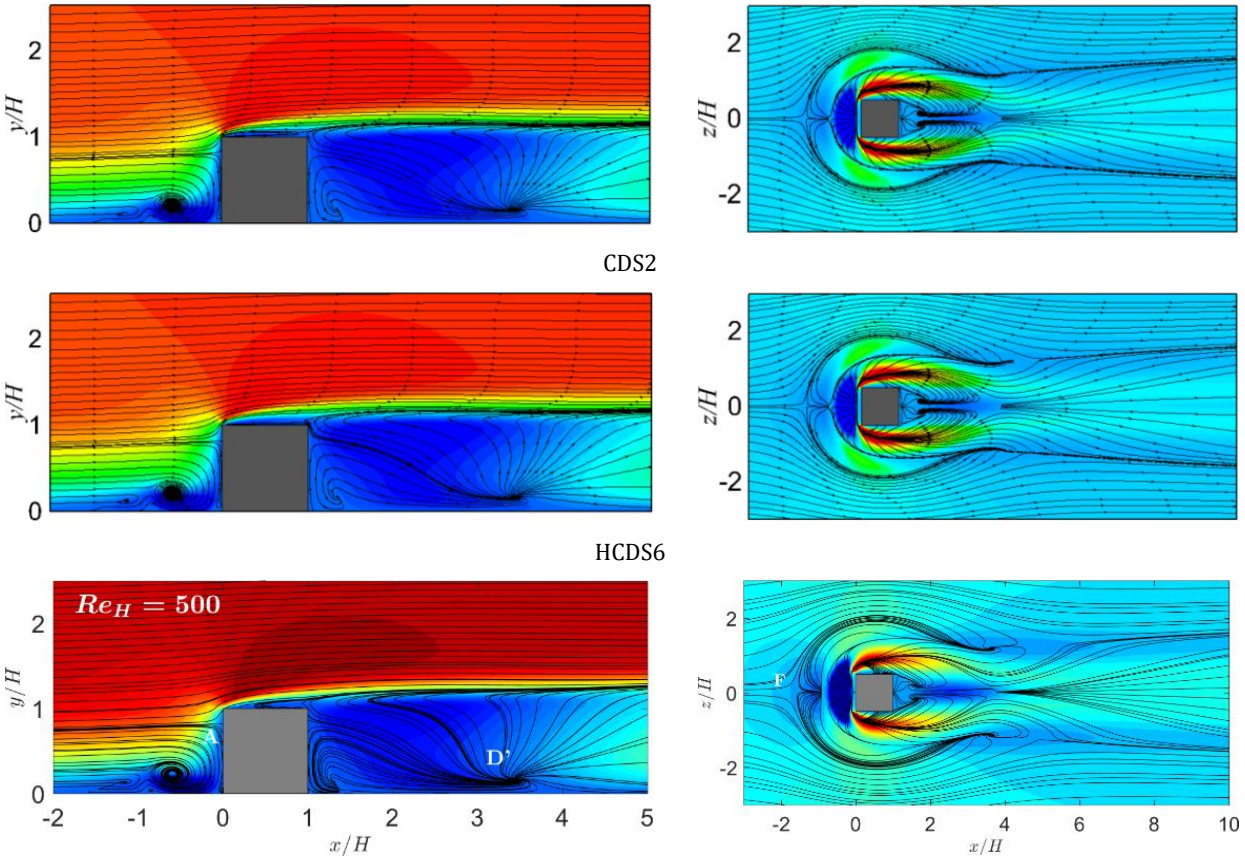

Reference DNS "Diaz-Daniel, Carlos, Sylvain Laizet, and J. Christos Vassilicos, International Journal of Heat and Fluid Flow, Vol.68, 2017; licensed under a Creative Commons Attribution (CC BY) license." [56]

Figure 2. Time-averaged streamwise velocity contours with mean flow streamline around a wall-attached cube at $Re_H = 500$. Left: $x - y$ plane, right: $x - z$ plane. The color scale for $\bar{u}$ spans from $-0.1U_\infty$ in dark blue to $1.1U_\infty$ in dark red for left column and $0.2U_\infty$ in dark red for right column.

A key flow diagnostic is the location of stagnation points, which provides a basis for a quantitative comparison between REEF3D and DNS reference solutions. The upstream stagnation point on the cube front face is marked A while the other one positioned farther from the front face is labeled F (see Figure 2, last row). The one that exists downstream is marked D. The location of stagnation points is reported in Table 4. Again, the results of the reference DNS solution [56] are accurately replicated. In this case, the mesh is conformal with the channel but non-conformal for the cube. This demonstrates that IBM is an accurate alternative to boundary-fitted meshes.

Table 4. Positions of stagnation points for the mean flow around the wall-attached cube immersed in a laminar boundary layer.

		y_A	x_D	y_D	x_F
Incompact3d [56]		0.82	3.48	0.17	−1.6
REEF3D (CDS2)	Enhanced direct forcing IBM approach	0.82	3.48	0.16	−1.5
REEF3D (HCDS6)		0.82	3.48	0.17	−1.5
REEF3D (CDS2)	Local directional ghost cell approach	0.82	3.48	0.16	−1.5
REEF3D (HCDS6)		0.82	3.48	0.17	−1.5

4.2 Steady non-axisymmetric flow past a sphere

The flow of a viscous fluid past a stationary sphere can trigger instabilities with three-dimensional flow patterns, despite the body symmetry. However, unlike two-dimensional flows, such three-dimensional patterns introduce a level of complexity that is characterized by wake formation and vortical interactions. Despite its apparent simplicity, this scenario represents a canonical problem in the family of immersed bluff body flows with numerous applications. The position of flow separation on a wall-mounted cube is mostly determined by the geometry, whereas, for a smooth surface like a sphere, it is primarily influenced by the pressure gradient and surface curvature. This benchmark is extensively documented in scientific literature [57-59].

An enhanced direct forcing IBM and local directional ghost cell approaches implemented in the REEF3D framework are used to simulate the flow at $Re_D = 250$ (based on the free stream velocity U_∞ and the sphere diameter D) in a steady laminar regime. A large computational domain of $[-10D, 10D]$ is considered in all three spatial directions. The sphere center is positioned at a distance $8D$ from the inlet. A uniform grid spacing of $0.02D$ is generated within a rectangular refinement zone of $[4D \times 2D \times 2D]$ surrounding the sphere. To limit the mesh size, the cells are stretched with a growth ratio of 1.25 between the refined zone and the domain external boundaries, where the maximum cell size is $0.2D$. A Dirichlet boundary condition $u/U_\infty = 1$, $v = 0$ and $w = 0$ is applied at the inlet and an outflow condition is imposed at the outlet boundary. A symmetry boundary condition is adopted for lateral directions, while a no-slip boundary condition is enforced on the sphere. To assess the performance of the numerical method, the drag (C_D) and lift (C_L) coefficients are compared with experimental data by Johnson and Patel [58]:

$$C_D = \frac{F_x}{\frac{1}{2}\rho U_\infty^2 \frac{\pi D^2}{4}} \tag{18}$$

$$C_L = \frac{F_y}{\frac{1}{2}\rho U_\infty^2 \frac{\pi D^2}{4}} \tag{19}$$

In Table 5, the results for drag and lift coefficients using both the standard second-order central differential scheme (CDS2) and the pseudo sixth-order central scheme (HCDS6) are presented. In the case of axisymmetric flow, the lift coefficient is naturally zero. Compared to the experimental data, the current approach can accurately compute steady drag and lift coefficients.

Table 5. Drag and lift coefficients for a flow past a sphere at $Re_D = 250$.

$Re_D = 250$	Method	C_D	C_L
Johnson and Patel [58]		0.7	0.062
REEF3D (CDS2)	Enhanced direct forcing IBM approach	0.7	0.054
REEF3D (HCDS6)		0.7	0.062
REEF3D (CDS2)	Local directional ghost cell approach	0.69	0.055
REEF3D (HCDS6)		0.68	0.059

For a qualitative comparison of this non-axisymmetric flow, the streamlines of projected streamwise velocity in the $(x - z)$ and $(y - z)$ planes are shown in Figure 3. Although the flow is steady state, it is non-axisymmetric at $Re_D = 250$ with a plane of symmetry. The present IBM correctly replicates the streamlines center compared to Johnson and Patel [58]. The length of the recirculation bubble and the location of the vortex center are well reproduced. To capture the wake structure correctly, the location of the boundary layer separation must be predicted accurately, which is not trivial as the sphere geometry has a smooth curve. Even though the mesh was isotropic and non-body conformal, the IBM method was able to predict this phenomenon correctly. This is important for building applications as some moving objects, such as occupants, present similar flow characteristics.

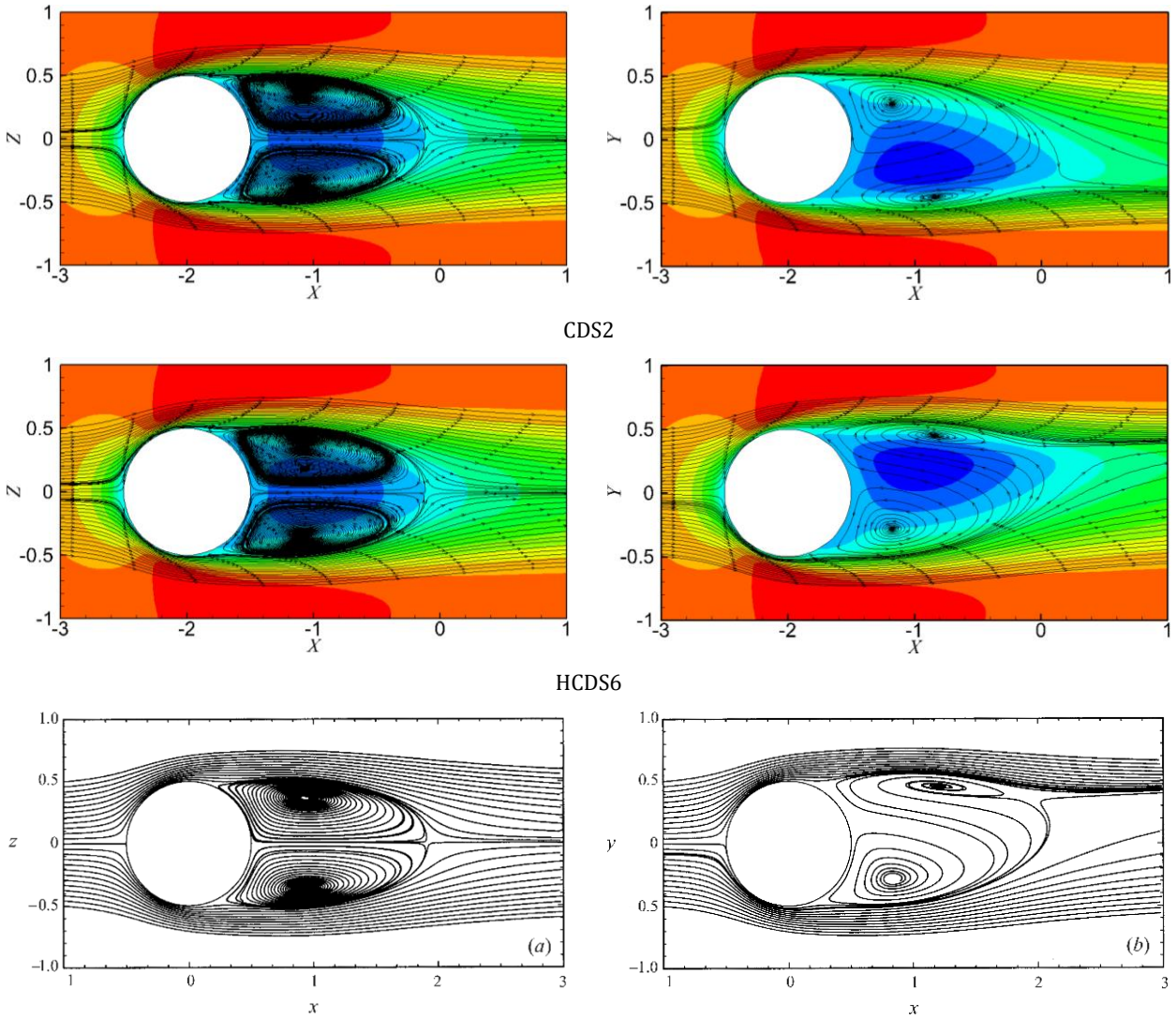

Reference "Reproduced with permission from J. Fluid Mech. (1999), vol. 378, pp. 19–70. Copyright 1999 Cambridge University Press." [58]

Figure 3. Streamlines of projected streamwise velocity for a flow past a sphere at $Re_D = 250$.

4.3 Flow past a sphere at higher Reynolds numbers (Re = 3700)

As the Reynolds number increases, the flow around the sphere loses the axisymmetry and steadiness. At sub-critical Reynolds numbers, the flow is unsteady and characterized by periodic shedding of vortices in the wake.

The performance of the numerical framework is analyzed for the flow past a sphere at the Reynolds number $Re_D = 3700$. The LES with WALE SGS model is performed to investigate the dynamics of vortex shedding and wake instabilities compared to DNS data by Rodriguez et al. [60]. The boundary conditions remain the same as those applied for the $Re_D = 250$ case. However, the computational domain is modified to accommodate the higher Reynolds number flow, extending to $[-15D, 15D]$ in the x direction and $[-10D, 10D]$ in both the y and z directions. To capture the finer details of the turbulent wake, a uniform grid spacing of $0.01D$ is used within a refined rectangular zone measuring $[2.5D \times 1.2D \times 1.2D]$ around the sphere with the sphere's center located $13D$ downstream from the inlet. Beyond this refinement zone, the grid transitions smoothly to coarser resolutions. In the x direction, the mesh growth ratio is set to 1.05, while in the other direction, a growth ratio of 1.1 is applied. The maximum cell size at the outer boundaries is limited to $0.2D$. This configuration ensures sufficient resolution in the wake region while keeping the overall mesh size computationally manageable. The 3D computational mesh together with refinement around the sphere is depicted in Figure 4. The simulation presented here is performed on a grid comprising approximately 30.2 million cells.

The computational time step of $0.01D/U_\infty$ is chosen to accurately capture temporal fluctuations in the turbulent wake and shear-layer instabilities. The simulation is advanced in time until the flow reaches statistical stationarity flow conditions to ensure that initial transients are completely eliminated. Once this condition is achieved, the instantaneous data are collected and flow statistics are averaged over an extended time period to ensure statistical convergence. Time-averaging is performed over a sufficiently long interval, equivalent to $345D/U_\infty$ or hundreds of flow-through times (FTTs).

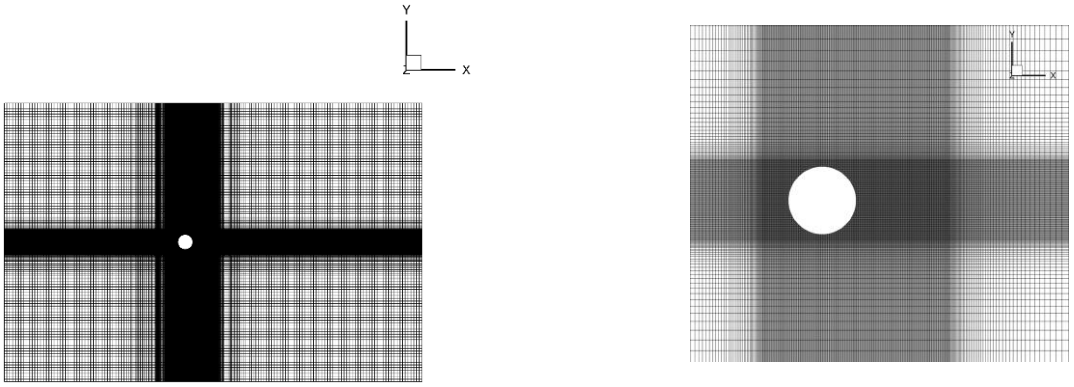

Figure 4. Computational domain and grid resolution.

The dominant frequencies associated with shear-layer instabilities and large-scale vortex shedding are identified through a spectral analysis of the y component velocity fluctuations. These fluctuations are sampled at multiple points in the near wake region. Probes are strategically placed, with one located near the axisymmetric shear layer at $x/D = 1, y/D = 0.6$ and another further downstream in the wake at $x/D = 5, y/D = 0.3$. The energy spectra are computed using time series data collected over a period of $345D/U_\infty$ to ensure sufficient resolution of flow dynamics across a wide range of frequencies. The results shown in Figure 5 reveal distinct frequency contributions at different locations. For instance, at $x/D = 5, y/D = 0.3$, a dominant peak corresponding to the vortex shedding frequency $St = fD/U_\infty = 0.215$, is observed in the spectrum. Further analysis highlights a high-frequency range near the shear layer, indicative of shear-layer instabilities, and a lower-frequency range downstream, corresponding to wake dynamics. In addition, the energy spectrum displays a $k^{-5/3}$ slope, as shown in Figure 5, aligning with Kolmogorov's theory.

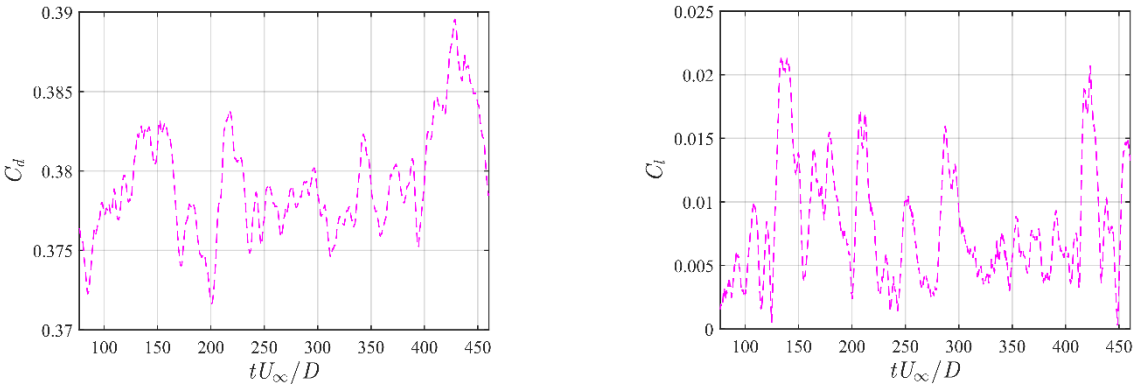

(a) (b)

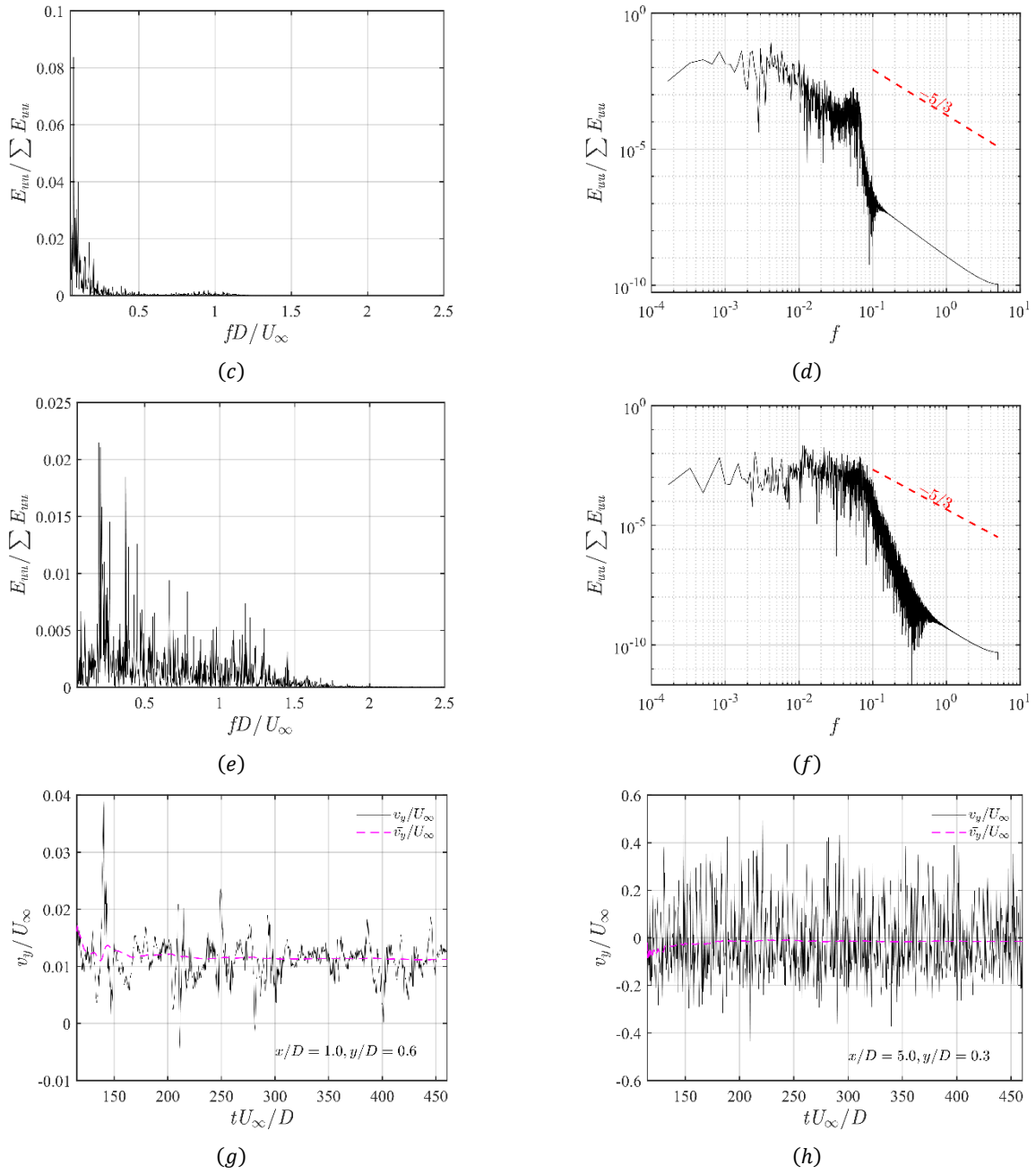

Figure 5. Time history and power spectrum at different locations (a, b) drag and lift coefficient, (c, d) power spectrum at $x/D = 1, y/D = 0.6$, (e, f) power spectrum at $x/D = 5, y/D = 0.3$, (g, h) y component velocity.

In Figure 6, the streamlines of projected mean streamwise velocity in the $(x - z)$ and $(y - z)$ planes are shown. In addition, the coherent vortical structures in the wake are visualized using Q-criterion iso-surfaces to identify the shear-layer instabilities and wake development behind and downstream of the sphere.

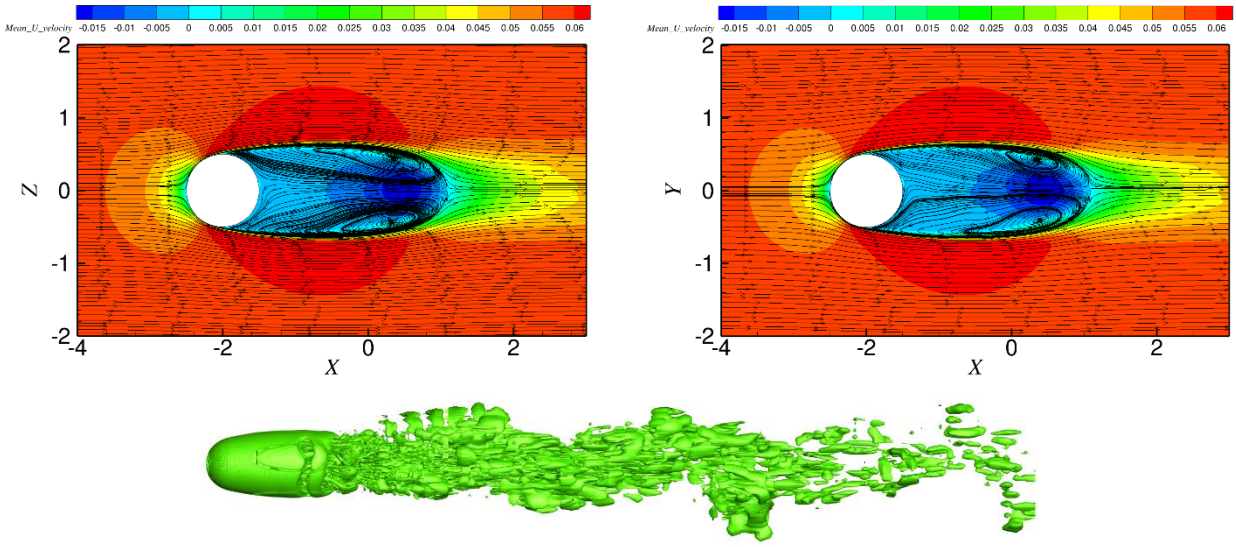

Figure 6. Streamlines of projected mean streamwise velocity (top) and instantaneous vortical structures (bottom) behind and downstream of the sphere at $Re_D = 3700$.

The time-averaged flow characteristics obtained from the simulation are summarized in Table 6. Key metrics, including the Strouhal number (St) associated with vortex-shedding frequency, the separation angle (ϕ_s) measured from the stagnation point, the normalized length of the recirculation bubble (L/D), and the mean drag coefficient $(\overline{C_d})$, are presented. For comparison, corresponding numerical results from the literature are also included.

Table 6. Statistical flow characteristics.

$Re_D = 3700$	Method	St	ϕ_s	$\overline{C_d}$	L/D
Rodriguez et al. [60]	DNS	0.215	89.4	0.394	2.28
Yun et al. [61]	LES	0.21	90	0.355	2.622
REEF3D (HCDS6)	Enhanced direct forcing IBM approach	0.211	89.5	0.38	2.59

The results show excellent agreement with previously reported data. For instance, the Strouhal number derived from the simulation is $St = 0.211$, which aligns closely with the experimentally reported range of 0.204 to 0.225 (e.g., [62, 63]). Similarly, the drag coefficient and recirculation bubble size exhibit consistency with benchmark studies, indicating the reliability of the numerical approach used.

4.4 LES of turbulent channel flow

In this section, the interaction of the numerical method with the SGS model is investigated using the wall-resolved turbulent channel flow benchmark. This evaluation is necessary to prove that explicit LES without artificial dissipation can be properly performed. Another objective is to demonstrate that the new proposed numerical scheme remains accurate and stable on a non-uniform mesh.

The LES of a turbulent channel flow at the frictional Reynolds number of $Re_\tau = 640$ is carried out. The WALE SGS model is adopted where the SGS kinematic viscosity is based on the invariants of the velocity gradient tensor [28]. This model recovers the proper y^3 near-wall scaling for turbulent eddy viscosity. Nicoud et al. [28] have calibrated the model coefficient in the range of $0.55 \leq C_w \leq 0.6$. However, this value is not universal and depends on the numerical method and Reynolds number. In the current case, the model coefficient value is calibrated to be $C_w = 0.46$. In this benchmark, a fully turbulent flow is developed between two infinite parallel plates separated by a distance 2δ. A constant adverse pressure gradient is applied to the flow in the streamwise direction to drive the flow through the channel. The no-slip condition is set for the top and bottom walls. Periodic boundary conditions are applied in the streamwise and spanwise directions to

approximate infinite homogeneous directions. The periodic domain sizes are selected so that the two-point correlations in the streamwise and spanwise directions would be essentially zero at maximum separation (half the domain size). A uniform grid is adopted in the periodic directions, whilst the grid is stretched in the direction normal to the wall in order to properly resolve the boundary layers. This grid-stretching is based on a hyperbolic tangent function:

$$y_j = -\frac{tanh\left(\gamma\left(1-\frac{2j}{N_y}\right)\right)}{tanh\,\gamma} \qquad j = 0,1,\ldots,N_y \tag{20}$$

where N_y is the number of grid points in the wall-normal direction, and γ is the stretching factor.

The computational domain size, grid resolution, and corresponding non-dimensional grid spacings in wall units are given in Table 7.

Table 7. Channel flow mesh resolution.

Re_τ	L_x	L_y	L_z	N_x	N_y	N_z	Δx^+	Δz^+	Δy^+	γ
640	$2\pi\delta$	2δ	$\pi\delta$	128	128	128	31.6	15.8	$\in [0.43 - 29.7]$	2.8

The computational domain is initialized with a random solenoidal velocity field. The bulk time scale $(t^* = L_x/U_b)$ is equivalent to a flow-through time (FTT) of the domain, which corresponds to the time it takes for the fluid to traverse the entire computational domain at a constant mean bulk velocity (U_b). A small time step is selected to capture temporal scales precisely and keeps the Courant number below one, thereby guaranteeing numerical stability. Once the flow has reached a statistical steady state condition, the flow statistics are averaged in the streamwise and spanwise homogeneous directions over a time interval of $50\delta/u_\tau$ approximately equivalent to 175 FTT, thereby ensuring fully converged statistics.

The mean streamwise velocity profile (U^+), the total Reynolds shear stress (T_{xy}), and the square root of the second-order velocity moments normalized by the friction velocity are shown in Figure 7 as a function of the dimensionless distance to the wall (y^+). The HCDS6 solution is in excellent agreement with the reference DNS results of Abe et al. [64]. The mean total Reynolds shear stress using both central schemes compares relatively well with the DNS data shown in the top-right graph in Figure 7. Moreover, the predictions for the spanwise (w_{rms}) and wall-normal (v_{rms}) turbulence-intensity components overlap with the reference DNS [64]. However, the streamwise component (u_{rms}) exhibits a slight deviation for y^+ above 60 when CDS2 is employed. In conclusion, these predictions confirm the consistency of the explicit LES approach followed in the paper, where no artificial numerical dissipation competes with the dissipation of the SGS model.

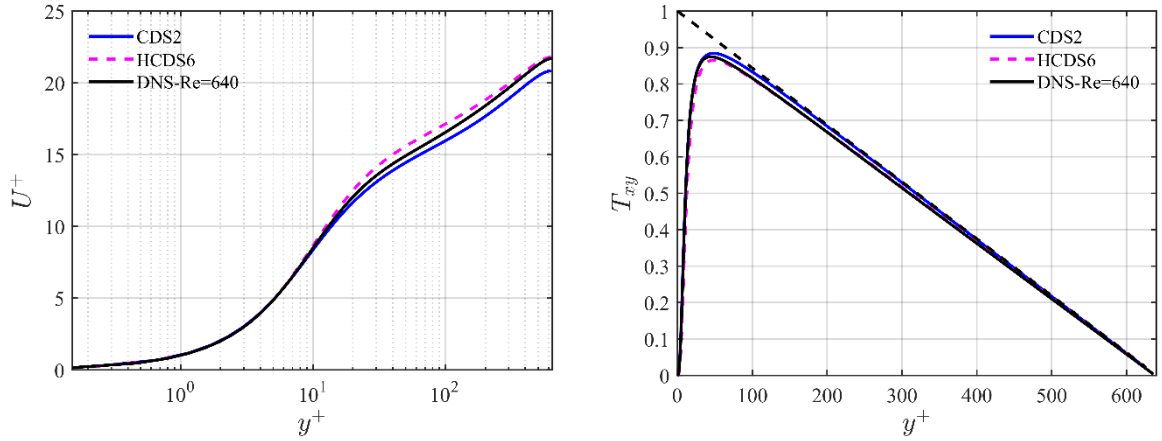

(a) (b)

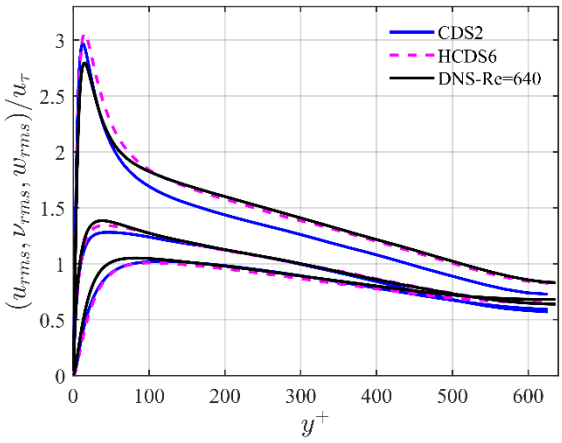

(c)

Figure 7. Mean streamwise velocity normalized by the DNS shear velocity (a), non-dimensional mean total Reynolds shear stress (b), mean normalized square root of the second-order velocity moments (c) (u_{rms} (top), v_{rms} (middle), w_{rms} (bottom)) for the LES of turbulent channel flow at $Re_\tau = 640$.

4.5 LES of the contaminant breach in isolation rooms with a sliding door

In the final test case, the potential of the framework introduced in Section 2 and its implementation in the REEF3D solver for indoor airflow applications are investigated.

Containment failure due to the airflows induced by a door movement is a critical concern in environments requiring strict isolation measures, such as hospital isolation rooms. The door motion initiates complex airflow patterns that can lead to the escape of potentially contaminated air. This can be particularly vital in the presence of airborne pathogens, as it increases the risk of spreading infectious agents to adjacent spaces. Traditional hinged doors, commonly found in healthcare facilities, are known to exacerbate this issue. Sliding doors, on the other hand, have shown promise in mitigating containment failure by minimizing the airflows generated during operation. Understanding these airflow dynamics is necessary for designing effective containment strategies to ensure the safety of both patients and healthcare personnel. Although quantitative measurements such as tracer gas techniques offer valuable data on airflow leakage, they may provide limited insight into the detailed turbulent flow structures that are mainly developed within the doorway. Moreover, these experiments can be complex and costly in terms of instrumentation setup and data collection. Alternatively, the CFD modeling using the LES approach overcomes the challenges associated with experimental measurements. Detailed visualization of airflow patterns by eliminating the need for full-scale mock-ups and specialized instrumentation can be provided by CFD simulations. However, the accuracy and reliability of airflow predictions during sliding door operations depends on the chosen numerical method.

The flow induced by a sliding door has been investigated by Saarinen et al. [40] through laboratory experiments as well as LES using ANSYS CFX 15.0. They demonstrated that URANS was not able to predict this flow accurately. The same setup of their test cases is used here, and their solution is taken as a reference (both experimental and numerical). Two identical isothermal rooms (the isolation room and the anteroom) without ventilation are connected via a sliding door in the middle of a partition wall. The dimensions of each room are $3.0 \times 4.7 \times 4.0\ m^3$ ($H \times W \times D$), as shown in Figure 8. The smallest width and height of the doorway are 1.1 and $2.06\ m$, respectively, with a frame thickness of $0.1\ m$. The door is $1.22\ m$ wide, $2.125\ m$ high, and has a thickness of $0.055\ m$.

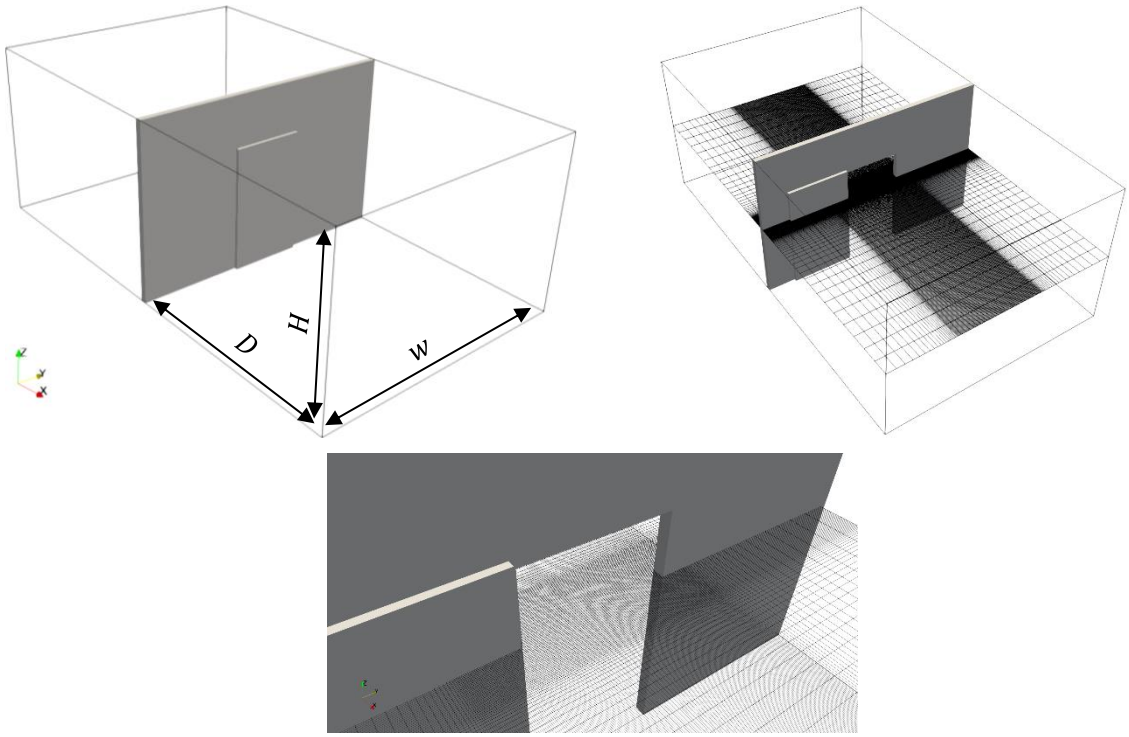

Figure 8. The computational grid (coarse) and geometry of the isolation room and anteroom connected via a sliding door.

The sequence of door operation involves two movement phases separated by a waiting period. First, the door slides open for a duration of three seconds, covering a distance of $1.2\ m$ linearly towards the negative y direction. The door is held fully open for nine seconds. Finally, it starts closing and reaches the initial position at a constant velocity after five seconds. The simulation is continued for a period of ten seconds to monitor the gradual airflow dissipation. The total time for the experiment is thus 27 seconds.

Similar to Saarinen et al. [40], the WALE SGS model is adopted in our simulation. To limit the mesh size, the computational grid is refined uniformly within a volume of $[x = 0.4\ m \times y = 1.5\ m \times z = 2.2\ m]$ surrounding the doorway where the unsteady vortical structures are generated. As illustrated in Figure 8, a smooth transition is performed away from the refined zone up to the domain boundaries with a growth ratio of 1.15. To study grid independence, four different grid resolutions of $\Delta x = \Delta y = \Delta z = 0.0025,\ 0.005,\ 0.00625$, and $0.01\ m$ are adopted in the refined volume for the ultrafine, fine, intermediate, and coarse grid, respectively. A no-slip boundary condition is applied to the room walls, including the separating wall and sliding door. Zero velocity components are initialized everywhere within two rooms. Consequently, each room serves as a large reservoir, and the airflow patterns are solely driven by the door motion. A constant time step of $4\ ms$ is chosen to resolve temporal variation while ensuring the numerical stability of the simulation by maintaining the CFL below one.

To visualize the unsteady shear flow generated by the sliding door, the vertical component of vorticity derived from the lateral gradients of velocity components $(\nabla \times \boldsymbol{u})_z$ is shown in Figure 9. The vorticity field is depicted when the door has fully opened and is extracted on a plane $1\ m$ above the floor. The opening of the door generates a wake with flow instabilities. The LES performed by Saarinen et al. [40] using a fine grid is shown in Figure $9(h)$ and is in line with flow visualization during their experiments. REEF3D accurately reproduces all number of vortices generated within the doorway on both intermediate and fine mesh resolutions, particularly when the new spatial discretization scheme (HCDS6) is employed. It should be noted that a direct comparison of accuracy with the LES of Saarinen et al. [40] is not feasible, given their omission of information regarding mesh size near the door in their refined 15.6M nodes mesh. Nonetheless, the coarse mesh used in this study maintains an equivalent grid size of $0.01m$ in proximity to the door, akin to the 10.7M nodes mesh employed by Saarinen et al. [40]. On the coarse mesh resolution, the limitations of the bounded second-order central difference scheme in ANSYS Fluent and the CDS2 in REEF3D are evident in their inability to accurately represent main flow structures. In contrast, the HCDS6 scheme demonstrates a better capability to capture the main features of these structures, despite the presence of significant aliasing errors visible in the

form of waves. This is attributed to the coarse mesh used, particularly compared to the door width. Additionally, it is noteworthy that the HCDS6 scheme, without artificial numerical dissipation, contributes to the observed aliasing errors (visible in the form of small waves). With further mesh refinement to a cell size of $0.00625m$ in the refined zone (intermediate mesh), the performance of the CDS2 scheme exhibits significant improvement. Compared to the coarse grid, it now demonstrates enhanced capability in capturing vortices within the doorway. Despite this improvement, some residual aliasing errors are still noticeable in the solution. Conversely, when employing the HCDS6 scheme on the intermediate mesh, aliasing errors are considerably reduced, resulting in a smoother visualization of the interaction of vortices. Although the solution of Saarinen et al. [40] reveals improved capture of vortices on a fine mesh (Figure $9(h)$), the solution remains somewhat inaccurate. Some details are still smeared when compared with the HCDS6 solution (Figure $9(d)$). Even with further improvements in the CDS2 solution on our fine mesh, which are achieved by reducing aliasing errors and refining the vortical structure shape, it remains incapable of accurately reproducing the correct position of rotational structures.

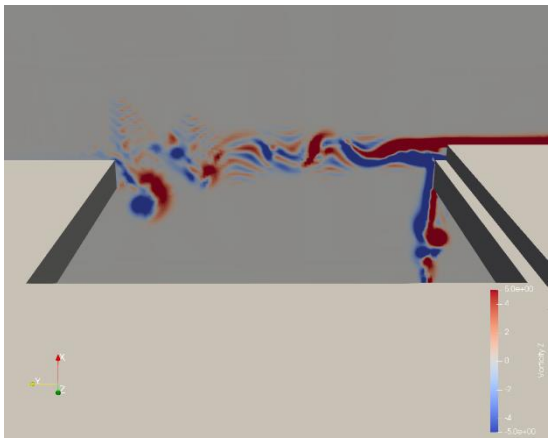

(a) CDS2 (coarse mesh)

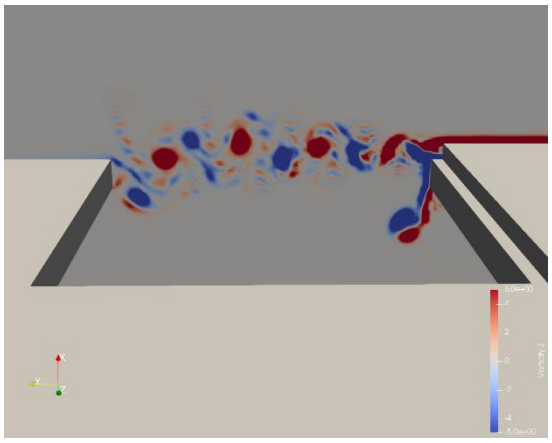

(b) HCDS6 (coarse mesh)

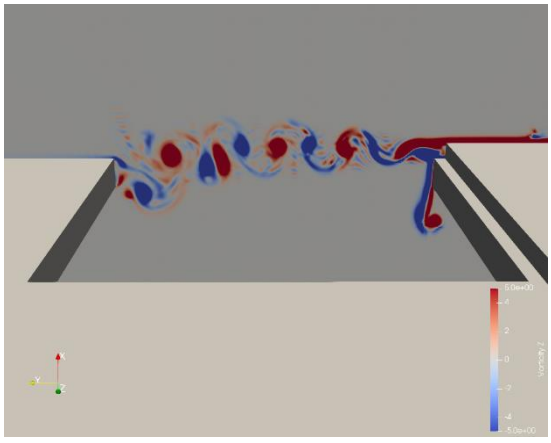

(c) CDS2 (intermediate mesh)

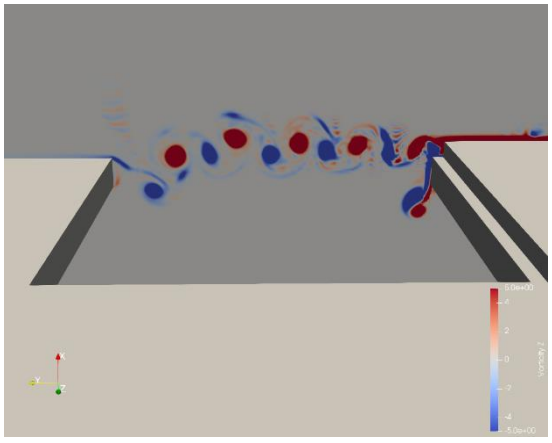

(d) HCDS6 (intermediate mesh)

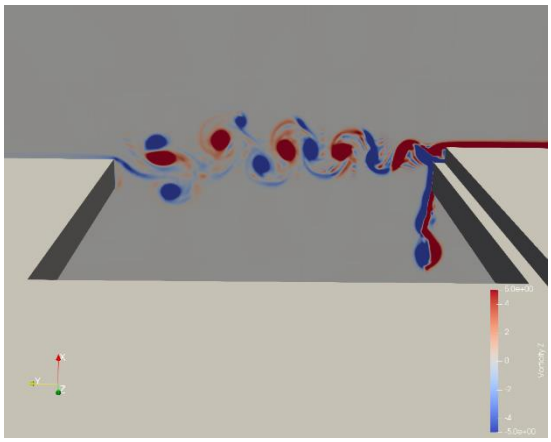

(e) CDS2 (fine mesh)

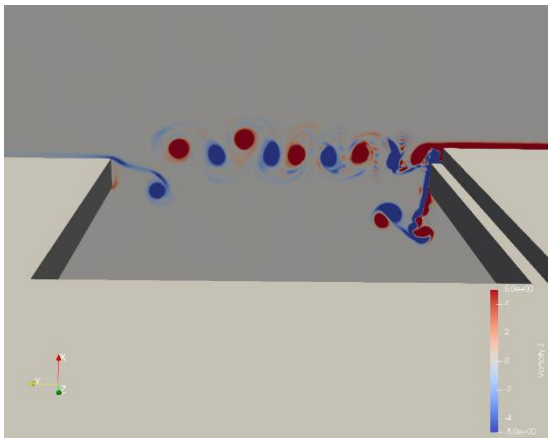

(f) HCDS6 (fine mesh)

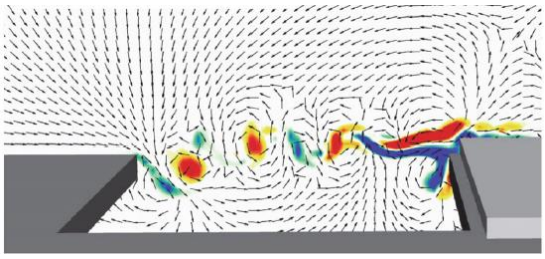

(g) Saarinen et al. "Reproduced with permission from Building Simulation (2018) 11: 585–596. Copyright 2017 Springer Nature." [40] (10.7M nodes)

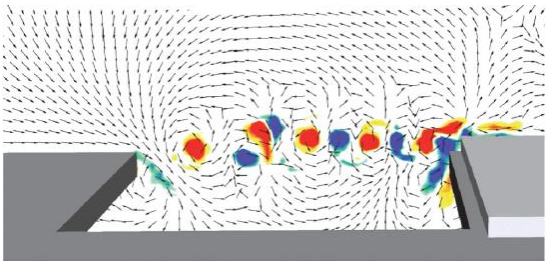

(h) Saarinen et al. "Reproduced with permission from Building Simulation (2018) 11: 585–596. Copyright 2017 Springer Nature." [40] (15.6M nodes)

Figure 9. Contours of the vertical component of vorticity $(\nabla \times \boldsymbol{u})_z$ at the end of door opening stage.

The flow dynamics induced by door motion in the proximity of the doorway can be visualized in detail using tracer gas. To compare with experiments, Saarinen et al. [40] modeled tracer gas as a passive scalar with a kinematic diffusivity of $1e-5\ m^2/s$ [65]. The turbulent Schmidt number (Sc) was set at a value of 0.9 to treat turbulent diffusive flux. The volume of air passing through the doorway from the isolation room to the anteroom as a function of time during the door cycle can be calculated using a gaseous contaminant dosed in the isolation room:

$$\Delta V(t)_{\text{isolation room}\rightarrow\text{anteroom}} = \frac{\Delta m(t)}{C_{\text{isolation room}}(t_0)} \tag{21}$$

The migrated mass of the gaseous contaminant (Δm) is obtained by integrating the tracer mass concentration (C) over the volume of anteroom:

$$\Delta m(t)_{\text{isolation room}\rightarrow\text{anteroom}} = \iiint_V^{anteroom} C(x,y,z,t)dV \tag{22}$$

Time evolution of air volume migration (AVM) quantifies how rapidly the air volume in the isolation room is escaping to the anteroom at different phases of the door cycle. The amount of air volume migrated from the isolation room to the anteroom over time is plotted in Figure 10 for the different grid sizes.

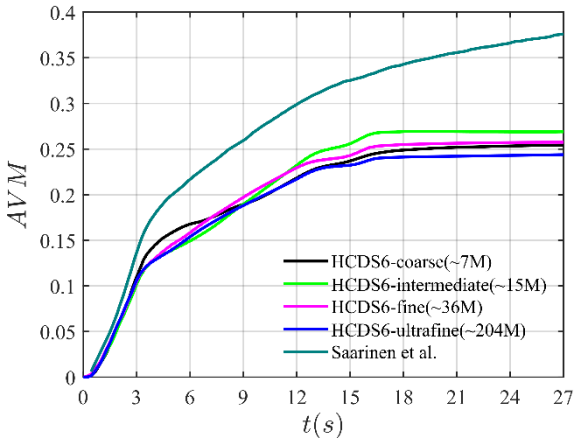

Figure 10. Time evolution of the air volume migrated during the sliding door operation cycle.

The flow instabilities near the doorway trigger the migration flow rate in the initial stage of the door opening. The intense volume of air passing through the doorway from the isolation room to the anteroom at the beginning can also be attributed to the piston effect induced by the moving door sliding within the anteroom. Consequently, the AVM increases quickly from 0 to 3 seconds when the door opens. The solution for the HCDS6 is identical during this opening phase for the four meshes. During the waiting period, when the sliding door is held open, a gradual increase in the migrated air volume is predicted due to the diffusion of turbulent vortices induced by the opening door motion. Consequently, the AVM continues to increase for the 9 seconds during which the door is held open (until $t = 12s$). The rate of AVM increase gradually diminishes over the subsequent 5 seconds as the door begins to close (until $t = 17s$). Once the door is fully closed, the AVM remains constant. It is worth noting that the AVM evaluated by Saarinen et al. [40] is very similar during the opening phase. However, after this phase, their predicted value is significantly higher than in our simulations. Surprisingly, their AVM keeps increasing when the door is closed after $t = 17s$ while it should remain constant as predicted by the present LES. It questions the conservation properties of scalar quantities in their numerical method including IBM.

In order to visualize the transient structures arising from the dynamic operation of the sliding door, Figure 11 presents contours of passive scalar concentration on a plane situated 1 m above the floor. These contours depict specific time intervals – namely, immediately after the door has fully opened ($t = 3s$), during the initial stages of closure ($t = 12s$), and after the door has completely closed ($t = 17s$). It is evident that the precision of the spatial discretization scheme to treat the convective term plays a key role in achieving an accurate solution. The HCDS6 scheme exhibits superior resolution of flow structures, leading to notable distinctions in flow patterns when compared to the CDS2 scheme over an extended duration. This highlights the advantage of employing an orthogonal grid, enabling the derivation of numerical schemes with enhanced accuracy, which is particularly beneficial for modeling transitional airflows within building environments.

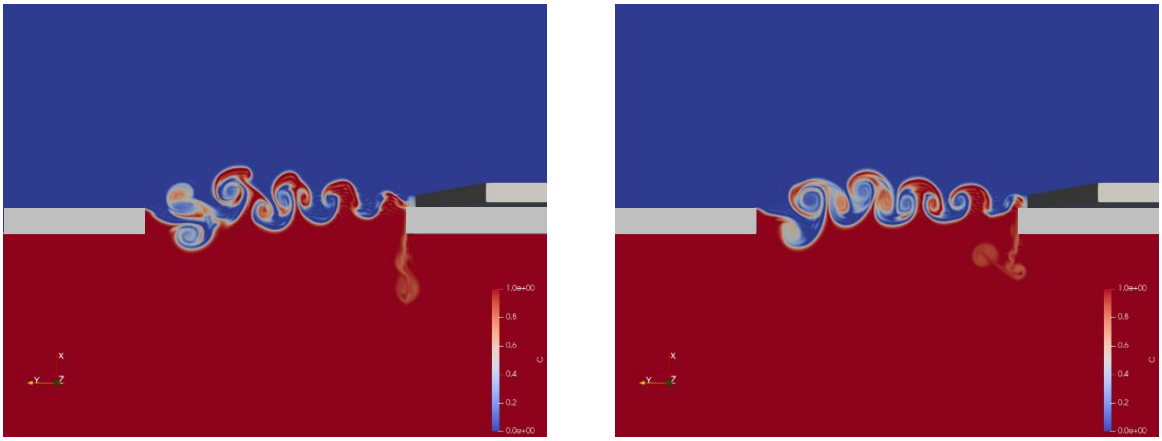

$t = 3s$

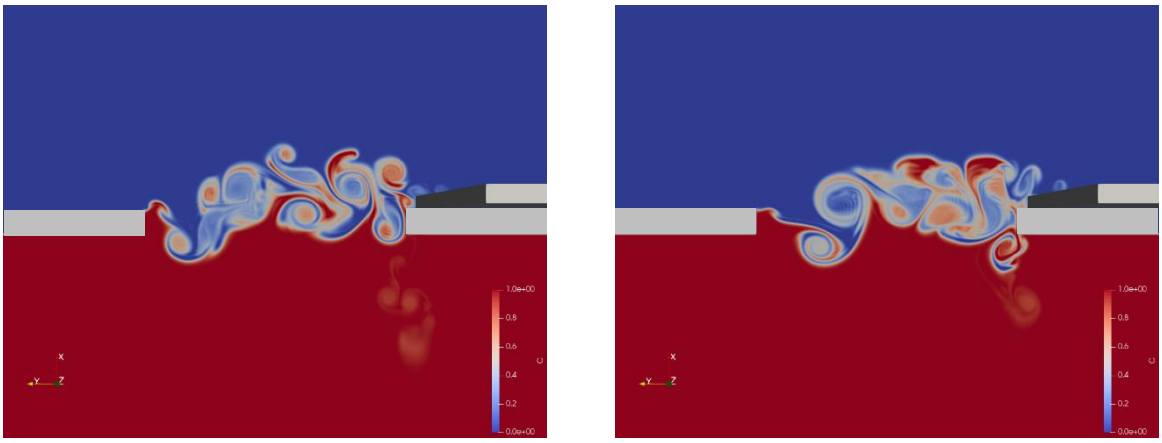

$t = 6s$

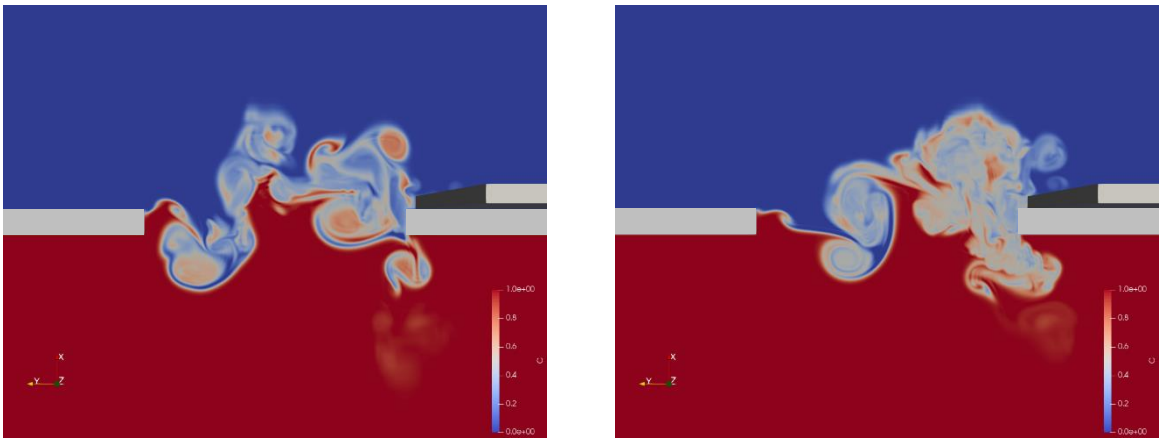

$t = 9s$

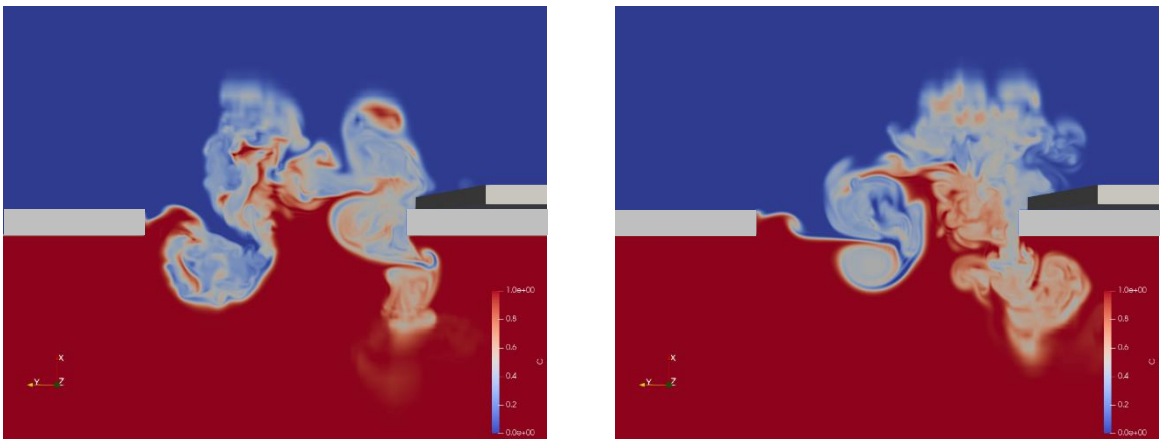

$t = 12s$

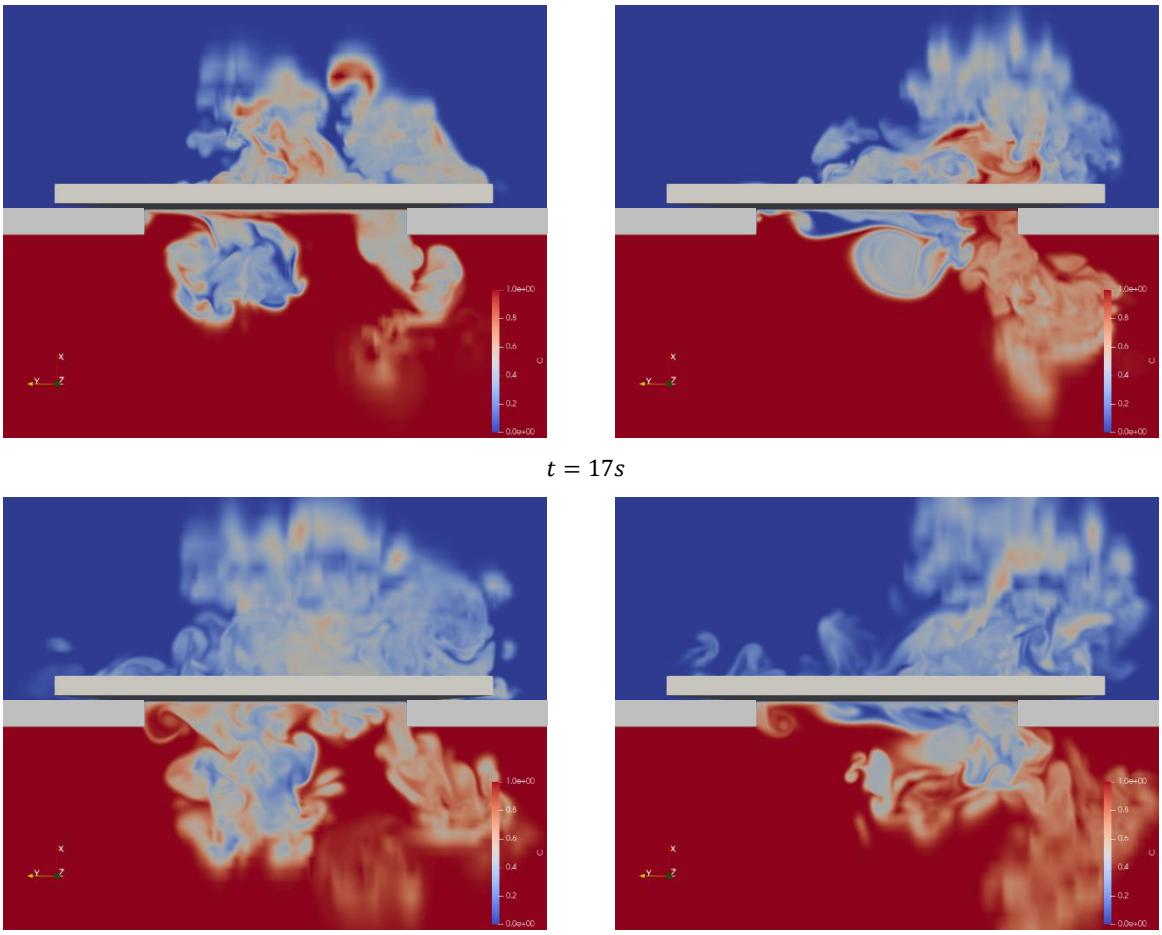

Figure 11. Contours of the passive scalar concentration at six different door opening stages using CDS2 (left) and HCDS6 (right).

5 Discussion

It is important to emphasize again that the proposed method targets indoor airflows. As recommended by Blocken [10], indoor and outdoor airflows should be clearly distinguished. The precision of capturing boundary layers becomes more crucial for outdoor airflows, which makes body conformal grids potentially more appropriate in such scenarios. The objective of this paper is not to assert the superiority of the current approach over widely-used general-purpose flow solvers such as ANSYS Fluent or OpenFOAM across all indoor airflow applications. These tools should be considered as alternatives, each with its own merits and limitations. Nevertheless, the article clearly highlights the benefits of the proposed framework, particularly in the context of high-resolution LES, transitional flows, and scenarios involving moving objects.

An essential consideration is computational time, which is an aspect that is not explicitly addressed and is not compared with general-purpose solvers in this article. The focus remains on showcasing that the proposed approach achieves comparable accuracy with fewer grid points than conventional flow solvers. The intricate nature of comparing computational times across different flow solvers necessitates dedicated benchmarks that offer a comprehensive description of simulation setups and parameters – an undertaking that is reserved for future endeavors.

Several paths can be followed for future research:

- While the five presented test cases serve to showcase the applicability of the framework within REEF3D for indoor airflow scenarios, additional test cases could provide deeper insights into its capabilities. Exploring scenarios involving thermal plumes, for instance, should be investigated, given their key role in indoor airflow dynamics [66]. One test case of a human thermal plume has been successfully validated by Choi et al. [38], using structured grids and IBM.

- Additionally, the resolution of the mesh was limited along the walls to maintain the feasibility of explicit time integration, thereby avoiding the need for semi-implicit methods. Future research should explore and assess the implementation of fully implicit time integration. In scenarios featuring airflow inlets, considerations for mesh refinement near these inlets, where the velocity magnitude is high, may be necessary. This is particularly relevant in cases such as a cavity flow with a slot inlet, where severe time step conditions must be observed based on the CFL criterion [67]. By employing an orthogonal mesh refined in the wall-normal direction, the high-velocity air entering through the slot will cross well-refined cells, thereby posing challenges to the time step due to the strict CFL condition. Adopting fully implicit time integration becomes a viable solution to release this constraint.
- Moreover, this study did not investigate cases with wall functions to assess the performance of wall-modeled LES. Future research should incorporate wall functions and analyze their impact on the simulation results. Finally, the sliding door case shows that aliasing errors may occur in highly under-resolved simulations with a pure central scheme (which is expected).
- In future work, the scheme could be complemented by a controlled amount of artificial numerical dissipation to address this phenomenon. As the numerical stencil has seven points in each spatial direction, it is indeed possible to tailor a high-order dissipation term (sometimes called hyperdiffusion term) that will only be active on the smallest resolved scales of the mesh, in line with the concept of explicit LES [68]. An example of such a hyper-dissipative term is the fifth-order scheme with a sixth-order spatial derivative of velocity in the flow solver PENCIL [69]. Such a hyperdiffusion term cannot be easily implemented in a general-purpose flow solver.

To conclude this section, information regarding the simulation platform and hardware is given. The current simulations were performed on the FRAM cluster provided by Sigma2, which is the National Infrastructure for High-Performance Computing and Data Storage in Norway. It is a distributed memory system that consists of 1,004 dual-socket and two quad-socket nodes, interconnected with a high-bandwidth, low-latency Infiniband network. The interconnect network is organized in an island topology, with 9,216 cores in each island. Each standard compute node has two 16-core Intel Broadwell chips (2.1 GHz) and 64 GB memory. In addition, eight larger memory nodes with 512 GB RAM are available, catering to computational tasks that demand substantial memory resources for more complex simulations and data-intensive processing. The total number of compute cores is 32,256.

6 Conclusions

The main objective of the paper was to discuss the use of solvers that are optimized for orthogonal non-conformal grids combined with the immersed boundary method (IBM) to perform high-resolution explicit LES for indoor airflows. This framework was then implemented by adapting an existing incompressible flow solver called REEF3D, which had initially been developed for hydrodynamics applications. It was shown that orthogonal grids enable the implementation of more accurate spatial discretization that outperforms the traditional second-order central scheme. This enabled the capturing of transitional flows using coarser meshes. Results showed that the immersed boundary method can capture the detached flow around an object with a smooth slope (i.e., a sphere) or sharp edges (i.e., a wall-mounted cube). The wall-resolved channel flow test case demonstrated that the numerical method was able to properly perform explicit LES. Finally, the sliding door test case demonstrated that IBM could simulate moving objects elegantly without resorting to complex re-meshing techniques. The superiority of high-accurate spatial discretization over standard second-order schemes on a same mesh is clearly shown. In further work, wall functions should be implemented to be able to address applications at higher Reynolds numbers, and the influence of these functions on the solution should be investigated.

Acknowledgments

The authors would like to acknowledge Iman Bayat for his assistance with language and proofreading during the research process.

This research did not receive any specific grant from funding agencies in the public, commercial, or not-for-profit sectors. The authors report there are no competing interests to declare. The authors have no conflicts to disclose.

Data availability statement

The data that support the findings of this study are available from the corresponding author, Elyas Larkermani, upon reasonable request.

Appendix

A.1 Time integration

To solve Equation (16) a predictor-corrector method is employed, as described in Section 3.4. The momentum predictor step (Equation (9)) is then performed without the forcing term to evaluate the intermediate field $\widehat{\boldsymbol{u}}^{\boldsymbol{m}}$. Forces acting on the discrete rigid body are computed, followed by solving the rigid body's equations of motion. Next, the rigid body position and its level set location are updated by transforming the coordinates of the triangles that define its discrete geometry. The intermediate rigid-body velocity field is then calculated based on the translational rigid-body velocity vector $(\dot{x})$, expressed in the inertial coordinate system, and the angular rigid-body velocity vector (ω_i), described using a body-fixed coordinate system.

$$\boldsymbol{P}(\hat{u}_i^m) = \dot{x} + \omega_i \times r \tag{23}$$

Here, r is the distance vector to the center of gravity of the rigid body. Hence, the forcing term is determined based on the updated values as:

$$f^m \approx \hat{f} = H(\hat{\varphi}_s^m) \cdot \frac{\boldsymbol{P}(\hat{u}_i^m) - \hat{u}_i^m}{\Delta t} \tag{24}$$

The forcing term is subsequently added to the intermediate velocity field. Following this step, the Poisson equation (Equation (11)) is solved, and with the pressure correction, the final velocity field is obtained (i.e., the correction step). Then the entire sequence is iterated over all stages of the Runge-Kutta method. Once complete, the algorithm advances to the next time step.

A.2 Level set method

The zero level set of the smooth signed distance function [70], as used for free surface representation, is adopted to identify the Fluid-Solid interface (Γ). The resulting properties of the level set function are as follows:

$$\varphi_s(\boldsymbol{x}, t) = \begin{cases} > 0 & \text{if } \boldsymbol{x} \in \text{fluid phase} \\ = 0 & \text{if } \boldsymbol{x} \in \Gamma \\ < 0 & \text{if } \boldsymbol{x} \in \text{solid phase} \end{cases} \tag{25}$$

The signed distance field (φ_s) is constructed using geometric data from an STL file, which represents the solid object as a collection of non-connected triangular elements [71]. The Eikonal equation guarantees that the level set function maintains its signed distance property, which is essential for mass conservation.

$$|\nabla \varphi_s| = 1 \tag{26}$$

In addition, the convection equation must be solved to track the evolution of the interface:

$$\frac{\partial \varphi_s}{\partial t} + \boldsymbol{u} \cdot \nabla \varphi_s = 0 \tag{27}$$

This equation uses the velocity field $(\boldsymbol{u})$, to update the level set function, ensuring it evolves consistently with the fluid flow. After each time step, the level set function must be reinitialized to preserve its signed distance property, particularly near the interface. This step prevents numerical errors that may accumulate during convection and ensures continued mass conservation. The reinitialization process is performed by solving a PDE-based reinitialization equation [72]:

$$\frac{\partial \varphi_s}{\partial t_p} + S(\varphi_s) \cdot (|\nabla \varphi_s| - 1) = 0 \tag{28}$$

Where t_p is the pseudo-time used for the reinitialization process and $S(\varphi_s)$ is a smoothed sign function [73]. Finally, the material properties of the two phases, such as density, are assigned using a smoothed transition across the interface, based on the level set function:

$$\rho = \rho_f H(\varphi_s) + \rho_s\big(1 - H(\varphi_s)\big) \quad (29)$$

Where the subscripts f and s denote fluid and solid phases, respectively. In the staggered grid method, the density and viscosity are required only at the cell faces rather than the cell centers. Consequently, these properties are directly evaluated at the faces to avoid unphysical oscillations caused by interpolation errors [46].

References

1. Tan, H., et al., *Current and potential approaches on assessing airflow and particle dispersion in healthcare facilities: a systematic review.* Environmental Science and Pollution Research, 2022. **29**(53): p. 80137-80160.
2. Löhner, R., et al., *High-fidelity simulation of pathogen propagation, transmission and mitigation in the built environment.* Archives of Computational Methods in Engineering, 2021. **28**: p. 4237-4262.
3. Lin, Y., et al., *A systematic review on COVID-19 related research in HVAC system and indoor environment.* Energy and Built Environment, 2023.
4. Chen, Q., *Ventilation performance prediction for buildings: a method overview and recent applications.* Building and Environment, 2009. **44**: p. 848-858.
5. Wang, L. and Q. Chen, *Evaluation of some assumptions used in multizone airflow network models.* Building and Environment, 2008. **43**(10): p. 1671-1677.
6. Megri, A.C. and F. Haghighat, *Zonal Modeling for Simulating Indoor Environment of Buildings: Review, Recent Developments, and Applications.* HVAC&R research, 2007. **13**(6): p. 887-905.
7. Teshome, E.J. and F. Haghighat, *Zonal Models for Indoor Air Flow: A Critical Review.* International Journal of Ventilation, 2004. **3**(2): p. 119-129.
8. Zuo, W. and Q. Chen, *Fast and informative flow simulations in a building by using fast fluid dynamics model on graphics processing unit.* Building and Environment, 2010. **45**(3): p. 747-757.
9. Zhai, Z.J., et al., *Evaluation of Various Turbulence Models in Predicting Airflow and Turbulence in Enclosed Environment by CFD: Part 1, Summary of Prevalent Turbulence Models.* HVAC&R Research, 2007. **13**(6): p. 853-870.
10. Blocken, B., *LES over RANS in building simulation for outdoor and indoor applications: A foregone conclusion?* Building Simulation, 2018. **11**(5): p. 821-870.
11. van Hooff, T., B. Blocken, and G.J.F. van Heijst, *On the suitability of steady RANS CFD for forced mixing ventilation at transitional slot Reynolds numbers.* Indoor Air, 2013. **23**: p. 236-249.
12. Coleman, G.N. and R.D. Sandberg, *A primer on direct numerical simulation of turbulence-methods, procedures and guidelines.* 2010.
13. Pham, M.V., F. Plourde, and K.S. Doan, *Direct and large-eddy simulations of a pure thermal plume.* Physics of Fluids, 2007. **19**.
14. Larkermani, E., G. Cao, and L. Georges, *Characterization of the density-driven counter-flow through a doorway using Large Eddy Simulation.* Building and Environment, 2022. **221**: p. 109319.
15. Wang, M. and Q. Chen, *Assessment of Various Turbulence Models for Transitional Flows in an Enclosed Environment (RP-1271).* HVAC&R Research, 2009. **15**(6): p. 1099-1119.
16. D. N. Sørensen, P.V.N., *Quality control of computational fluid dynamics in indoor environments.* Indoor Air, 2004. **13**(1): p. 2-17.
17. van Hooff, T., B. Blocken, and Y. Tominaga, *On the accuracy of CFD simulations of cross-ventilation flows for a generic isolated building: Comparison of RANS, LES and experiments.* Building and Environment, 2017. **114**: p. 148-165.
18. Zhang, Z., et al., *Evaluation of Various Turbulence Models in Predicting Airflow and Turbulence in Enclosed Environment by CFD: Part 2, Comparison with Experimental Data from Literature.* HVAC&R Research, 2007. **13**(6): p. 871-886.
19. Spalart, P.R. *Comments on the Feasibility of LES for Wings and on the Hybrid RANS/LES Approach*. in *Proceedings of the First AFOSR International Conference on DNS/LES, 1997*. 1997.
20. Spalart, P.R., *Hybrid RANS-LES Methods*, in *Advanced Approaches in Turbulence*. 2021, Elsevier. p. 133-159.
21. Verstappen, R.W.C.P. and A.E.P. Veldman, *Symmetry-preserving discretization of turbulent flow.* Journal of Computational Physics, 2003. **187**: p. 343–368.

22. Mahfoze, O.A. and S. Laizet, *Non-explicit large eddy simulations of turbulent channel flows from Reτ=180 up to Reτ=5,200.* Computers & Fluids, 2021. **228**: p. 105019.
23. Mittal, R. and G. Iaccarino, *Immersed Boundary Methods.* Annual Review of Fluid Mechanics, 2005. **37**(1): p. 239-261.
24. Bae, H.J., et al., *Dynamic slip wall model for large-eddy simulation.* Journal of fluid mechanics, 2019. **859**: p. 400-432.
25. Kawai, S. and J. Larsson, *Wall-modeling in large eddy simulation: Length scales, grid resolution, and accuracy.* Physics of fluids, 2012. **24**(1).
26. Lozano-Durán, A., et al., *Non-equilibrium three-dimensional boundary layers at moderate Reynolds numbers.* Journal of Fluid Mechanics, 2020. **883**: p. A20.
27. Chen, B., et al., *A new wall function for indoor airflow with buoyancy effect.* Building and Environment, 2021. **202**: p. 108029.
28. Nicoud, F. and F. Ducros, *Subgrid-scale stress modelling based on the square of the velocity gradient tensor.* Flow, turbulence and Combustion, 1999. **62**(3): p. 183-200.
29. Germano, M., et al., *A dynamic subgrid-scale eddy viscosity model.* Physics of Fluids A: Fluid Dynamics, 1991. **3**(7): p. 1760-1765.
30. Bricteux, L., M. Duponcheel, and G. Winckelmans, *A multiscale subgrid model for both free vortex flows and wall-bounded flows.* Physics of Fluids, 2009. **21**.
31. Jeanmart, H. and G. Winckelmans, *Investigation of eddy-viscosity models modified using discrete filters: A simplified "regularized variational multiscale model" and an "enhanced field model".* Physics of Fluids, 2007. **19**(5): p. 055110.
32. Joel H. Ferziger, M.P., Robert L. Street, *Computational Methods for Fluid Dynamics*. 4 ed. 2020: Springer Cham.
33. Komen, E.M.J., et al., *Analysis of the numerical dissipation rate of different Runge–Kutta and velocity interpolation methods in an unstructured collocated finite volume method in OpenFOAM®.* Computer Physics Communications, 2020. **253**: p. 107145.
34. Vasilyev, O.V., *High order finite difference schemes on non-uniform meshes with good conservation properties.* Journal of Computational Physics, 2000. **157**(2): p. 746-761.
35. Kempe, T. and A. Hantsch, *Large-eddy simulation of indoor air flow using an efficient finite-volume method.* Building and Environment, 2017. **115**: p. 291-305.
36. Morozova, N., et al., *On the feasibility of affordable high-fidelity CFD simulations for indoor environment design and control.* Building and Environment, 2020. **184**: p. 107144.
37. Mao, S. and I.B. Celik, *Modeling of indoor airflow and dispersion of aerosols using immersed boundary and random flow generation methods.* Computers & Fluids, 2010. **39**(8): p. 1275-1283.
38. Choi, J.-I. and J.R. Edwards, *Large-eddy simulation of human-induced contaminant transport in room compartments.* Indoor Air, 2012. **22**: p. 77-87.
39. Choi, J.-I. and J.R. Edwards, *Large eddy simulation and zonal modeling of human-induced contaminant transport.* Indoor Air, 2008. **18**: p. 233-249.
40. Saarinen, P., et al. *Large-eddy simulation of the containment failure in isolation rooms with a sliding door—An experimental and modelling study*. in *Building Simulation*. 2018. Springer.
41. Bihs, H. *REEF3D : Open-Source Hydrodynamics*. Available from: https://reef3d.wordpress.com/.
42. Kim, J. and P. Moin, *Application of a fractional-step method to incompressible Navier-Stokes equations.* Journal of Computational Physics, 1985. **59**(2): p. 308-323.
43. Falgout, R.D. and U.M. Yang. *hypre: A Library of High Performance Preconditioners*. in *Computational Science — ICCS 2002*. 2002. Berlin, Heidelberg: Springer Berlin Heidelberg.
44. Berthelsen, P.A. and O.M. Faltinsen, *A local directional ghost cell approach for incompressible viscous flow problems with irregular boundaries.* Journal of Computational Physics, 2008. **227**(9): p. 4354-4397.
45. Yang, L., *One-fluid formulation for fluid–structure interaction with free surface.* Computer Methods in Applied Mechanics and Engineering, 2018. **332**: p. 102-135.
46. Bihs, H., et al., *A new level set numerical wave tank with improved density interpolation for complex wave hydrodynamics.* Computers & Fluids, 2016. **140**: p. 191-208.
47. Kálnay de Rivas, E., *On the use of nonuniform grids in finite-difference equations.* Journal of Computational Physics, 1972. **10**(2): p. 202-210.
48. Morinishi, Y., et al., *Fully Conservative Higher Order Finite Difference Schemes for Incompressible Flow.* Journal of Computational Physics, 1998. **143**: p. 90-124.

49. Larkermani, E., et al., *Development of an accurate central finite-difference scheme with a compact stencil for the simulation of unsteady incompressible flows on staggered orthogonal grids.* Computer Methods in Applied Mechanics and Engineering, 2024. **428**: p. 117117.
50. Le, H. and P. Moin, *An improvement of fractional step methods for the incompressible Navier-Stokes equations.* Journal of Computational Physics, 1991. **92**(2): p. 369-379.
51. Van der Vorst, H.A., *Bi-CGSTAB: A fast and smoothly converging variant of Bi-CG for the solution of nonsymmetric linear systems.* SIAM Journal on scientific and Statistical Computing, 1992. **13**(2): p. 631-644.
52. Falgout, R.D., J.E. Jones, and U.M. Yang, *Conceptual interfaces in hypre.* Future Generation Computer Systems, 2006. **22**(1-2): p. 239-251.
53. Soydan, A., W.W. Wang, and H. Bihs. *An Upgraded Direct Forcing Immersed Boundary Method With Integrated Mooring Algorithm for Floating Offshore Wind Turbines*. in *International Conference on Offshore Mechanics and Arctic Engineering*. 2024. American Society of Mechanical Engineers.
54. Lin, Q., et al., *Large eddy simulations of strong wind mechanisms at pedestrian level around square-section buildings with same aspect ratios and different sizes.* Building and Environment, 2023. **243**: p. 110680.
55. Khaled, M.F. and A.M. Aly, *Assessing aerodynamic loads on low-rise buildings considering Reynolds number and turbulence effects: a review.* Advances in Aerodynamics, 2022. **4**(1): p. 24.
56. Diaz-Daniel, C., S. Laizet, and J.C. Vassilicos, *Direct numerical simulations of a wall-attached cube immersed in laminar and turbulent boundary layers.* International Journal of Heat and Fluid Flow, 2017. **68**: p. 269-280.
57. Ploumhans, P., et al., *Vortex methods for direct numerical simulation of three-dimensional bluff body flows: application to the sphere at Re= 300, 500, and 1000.* Journal of Computational Physics, 2002. **178**(2): p. 427-463.
58. Johnson, T. and V. Patel, *Flow past a sphere up to a Reynolds number of 300.* Journal of Fluid Mechanics, 1999. **378**: p. 19-70.
59. Choi, J.-I., et al., *An immersed boundary method for complex incompressible flows.* Journal of Computational Physics, 2007. **224**(2): p. 757-784.
60. Rodriguez, I., et al., *Direct numerical simulation of the flow over a sphere at Re= 3700.* Journal of Fluid Mechanics, 2011. **679**: p. 263-287.
61. Yun, G., D. Kim, and H. Choi, *Vortical structures behind a sphere at subcritical Reynolds numbers.* Physics of Fluids, 2006. **18**(1).
62. Kim, H. and P. Durbin, *Observations of the frequencies in a sphere wake and of drag increase by acoustic excitation.* The Physics of fluids, 1988. **31**(11): p. 3260-3265.
63. Sakamoto, H. and H. Haniu, *A study on vortex shedding from spheres in a uniform flow.* 1990.
64. Abe, H., R.A. Antonia, and H. Kawamura, *Correlation between small-scale velocity and scalar fluctuations in a turbulent channel flow.* Journal of Fluid Mechanics, 2009. **627**: p. 1-32.
65. Zhuang, R.N., X. Li, and J. Tu, *Should different gaseous contaminants be treated differently in CFD indoor simulations?* WIT Transactions on Ecology and the Environment, 2014. **183**: p. 353-362.
66. Sun, S., J. Li, and J. Han, *How human thermal plume influences near-human transport of respiratory droplets and airborne particles: a review.* Environmental Chemistry Letters, 2021. **19**(3): p. 1971-1982.
67. Nielsen, P.V., A. Restivo, and J.H. Whitelaw, *The Velocity Characteristics of Ventilated Rooms.* Journal of Fluids Engineering, 1978. **100**(3): p. 291-298.
68. Kritsuk, A.G., et al., *High order nonlinear filter methods for subsonic turbulence simulation with stochastic forcing.* Journal of Computational Physics, 2021. **431**: p. 110118.
69. Haugen, N.E.L. and A. Brandenburg, *Inertial range scaling in numerical turbulence with hyperviscosity.* Physical Review E, 2004. **70**(2): p. 026405.
70. Osher, S. and J.A. Sethian, *Fronts propagating with curvature-dependent speed: Algorithms based on Hamilton-Jacobi formulations.* Journal of computational physics, 1988. **79**(1): p. 12-49.
71. Chua, C.K., K.F. Leong, and C.S. Lim, *Rapid prototyping: principles and applications*. 2010: World scientific.
72. Sussman, M., P. Smereka, and S. Osher, *A level set approach for computing solutions to incompressible two-phase flow.* Journal of Computational physics, 1994. **114**(1): p. 146-159.
73. Peng, D., et al., *A PDE-based fast local level set method.* Journal of computational physics, 1999. **155**(2): p. 410-438.